UNIVERSITY OF CALIFORNIA SAN DIEGO

Pushing the Bounds of Halide Perovskite Solar Cell Stability using a Streamlined, Automated Platform for Fabrication and Testing

A Thesis submitted in partial satisfaction of the
requirements for the degree Master of Science

in

NanoEngineering

by

Ken Kaushal

Committee in charge:

Professor David P. Fenning, Chair
Professor Oscar Vazquez Mena
Professor Donald Sirbuly

2024

The Thesis of Ken Kaushal is approved, and it is acceptable in quality and form for publication on microfilm and electronically.

University of California San Diego

2024

TABLE OF CONTENTS

LIST OF FIGURES

LIST OF TABLES

ACKNOWLEDGEMENTS

I wish to extend my deepest gratitude to Professor David P. Fenning for giving me the opportunity to be part of his research team. His exceptional patience and mentorship have been invaluable to my development, and his infectious enthusiasm for our research has continually inspired me.

ABSTRACT OF THE THESIS

Pushing the Bounds of Halide Perovskite Solar Cell Stability using a Streamlined, Automated Platform for Fabrication and Testing

by

Ken Kaushal

Master of Science in NanoEngineering

University of California San Diego, 2024

Professor David P. Fenning, Chair

With global efforts transitioning toward renewable energy, solar power holds immense potential for reliable electricity generation. Metal halide perovskites have emerged as promising photovoltaic semiconductors due to their remarkable optoelectronic properties, including high absorption coefficients, tunable bandgaps, and high charge carrier mobility. In addition, low-temperature solution processing offers advantages in cost and scalability. However, their susceptibility to degradation under operating conditions remains a barrier to widespread commercialization. This thesis reports on high-throughput research enabled by streamlining and adding capabilities to the existing automated fabrication and characterization setup at the Solar Energy

Innovation Lab. Additionally, three distinct approaches were explored to improve perovskite solar cell performance and stability: (1) cationic substitution for lattice stabilization, (2) intermediate phase promoting additives to enhance perovskite film crystallization, and (3) metal oxide nanoparticle-based charge transport layers for optimized band alignment and higher open-circuit voltage. Finally, contributions towards developing international standard compliant degradation testing facilities is presented.

Chapter 1

The Pressing Need for Terawatt Scale Solar Energy; Metal Halide Perovskites as a Promising Photovoltaic Material

1.1 Facing the Climate Crisis

The Earth's climate is changing at an alarming rate, driven primarily by human activities. The Intergovernmental Panel on Climate Change (IPCC), the leading international body for the assessment of climate change, reports a global temperature rise of approximately 1.0°C above pre-industrial levels [22]. This seemingly small increase translates to a cascade of devastating consequences, including rising sea levels, more extreme weather events like heatwaves, droughts, floods, and intensified storms, and disruptions to precipitation patterns that threaten food security for millions [10].

The primary culprit behind these changes is the burning of fossil fuels—coal, oil, and natural gas—which release greenhouse gases like carbon dioxide into the atmosphere. These gases trap heat, causing a gradual warming effect. The International Energy Agency (IEA) reports that fossil fuels still dominate the global energy landscape, accounting for a staggering 80% of global energy consumption in 2023 [14]. This dependence on fossil fuels creates a vicious cycle: the more energy we consume, the more greenhouse gases we emit, further accelerating climate change. Despite a growing focus on cleaner energy sources, the United States remains

heavily dependent on fossil fuels. According to the U.S. Energy Information Administration (EIA), natural gas reigns supreme in the U.S. electricity grid (Figure 1.1), contributing roughly 38% of generation in 2022 [39]. Coal and nuclear power also play significant roles, together providing nearly 47% of U.S. electricity generation in 2022. Renewable energy sources like wind and solar are far behind, collectively providing 25% of U.S. electricity generation in 2022.

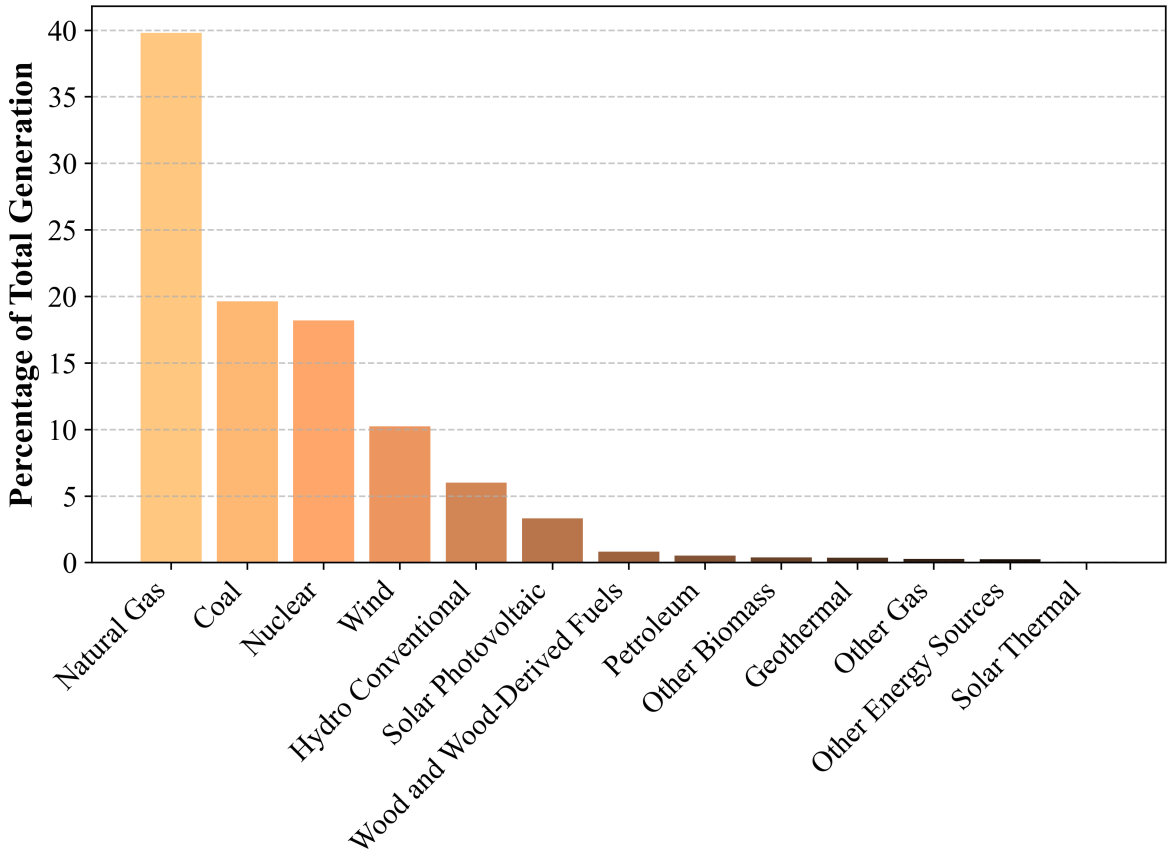

Figure 1.1. United States 2022 Utility scale energy generation by source

The international community recognizes this colossal gap in most countries and the urgency to address this situation. The Paris Agreement, adopted by nearly every nation in 2015, sets a global goal of limiting warming to well below 2°C, preferably to 1.5°C, compared to pre-industrial levels [36]. Achieving this ambitious target requires a rapid and decisive shift towards clean energy sources. Additionally, The United States has pledged significant cuts in

greenhouse gas emissions as part of its commitment to the Paris Agreement. The Environmental Protection Agency (EPA) outlines an ambitious goal of achieving a 50-52% reduction in net greenhouse gas emissions from 2005 levels by 2030 [37]. Achieving this target would require a monumental transformation of the US energy sector, with a significant increase in the adoption of clean energy sources like solar power.

The Department of Energy (DOE) is therefore taking bold steps towards a clean energy future. In May 2023, Secretary Granholm announced a department goal of achieving a 100% carbon-free electricity sector by 2035 [38]. This ambitious target underscores the urgency of developing and deploying clean energy technologies at scale.

1.2 Exploring Solar Energy: Unveiling Potential, Addressing Challenges

Solar energy emerges as a beacon of hope at this critical juncture. The Sun continuously bathes our planet in an extraordinary amount of clean and sustainable energy. According to NASA's Langley Research Center, the Earth intercepts a staggering 173,000 terawatts (TW) of solar irradiation on average each day [27]. This amount is so vast that it dwarfs our current global energy consumption of around 18 TW [14]. Capturing even a small fraction of this abundant resource could revolutionize our energy landscape and significantly reduce our reliance on fossil fuels. Roughly calculating, capturing just 1% of the sunlight reaching Earth would generate more than 17 times our current global energy needs. This immense potential underscores the critical role solar energy can play in addressing the climate crisis.

However, translating this potential into reality faces challenges. One significant hurdle is the vast area required to meet all our energy demands solely with current solar photovoltaic (PV) technology. Solar PV refers to the conversion of sunlight directly into electricity using solar cells made out of semiconductors. Commercially available solar cells are made of silicon, which is the photoactive semiconductor. These solar cells dominate around 90% of the market [26],

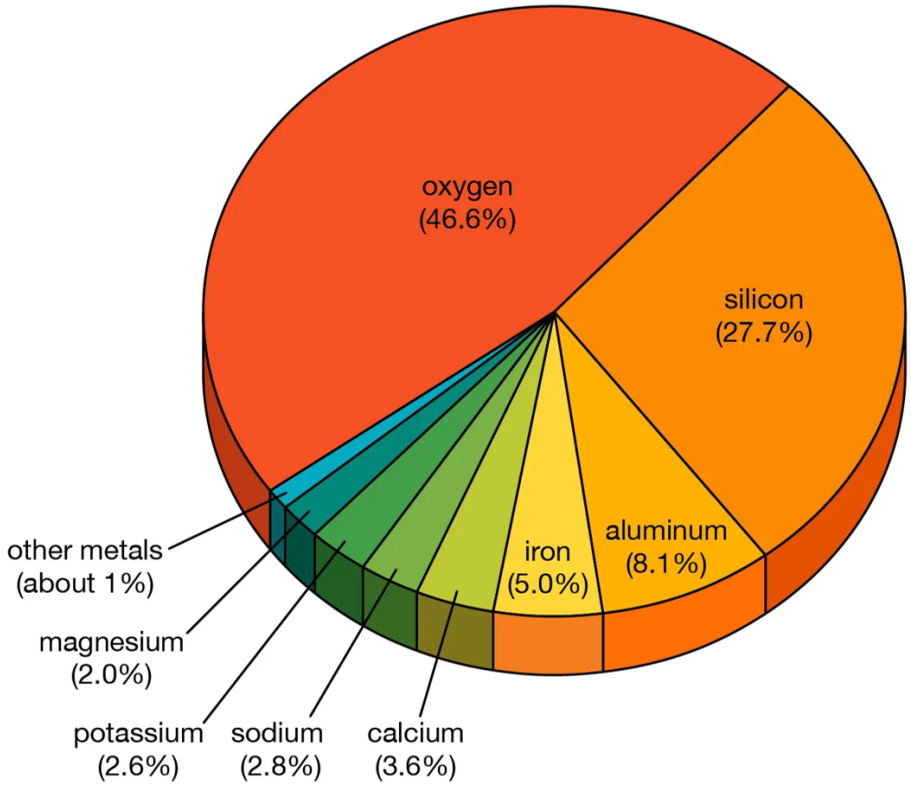

Figure 1.2. Percentage composition of the most common elements found in the earths crust

boasting an average efficiency of around 22%, meaning they can convert roughly 22% of the sunlight they receive into usable electricity. To meet the world's energy demands, roughly half of the Sahara's landmass would need to be covered in these solar panels.

While silicon is the second most abundant element on Earth [1], Figure 1.2, translating this abundance into a large-scale solution for solar energy presents significant challenges. The manufacturing process for silicon solar cells, which involves converting high-purity silicon from silicon oxide in the Earth's crust, requires extremely high temperatures, often achieved through energy-intensive processes relying on fossil fuels [34]. This creates a paradox: the production of solar panels to decarbonize our grid can itself contribute to greenhouse gas emissions. Additionally, these processes involve hazardous materials like silicon tetrachloride ($SiCl_4$), raising environmental and safety concerns.

Even after installation, the environmental impact of solar panels should be considered. A

key factor is the ”Energy payback time” - the amount of time it takes for a solar panel to generate enough energy to offset the energy consumed during its production and installation. While estimates vary, current silicon solar panels typically have an energy payback time of around 2-4 years [30]. Hence, it takes several years of operation before the clean energy generated by the panel outweighs the environmental impact of its creation. Silicon's inherent limitations as a semiconductor material restrict the efficiency of solar cells made from it. This bottleneck hinders the development of higher-efficiency cells, which could generate more energy and shorten the energy payback time.

1.3 Metal Halide Perovskites: A Promising Alternative to Silicon Solar Cells

Metal Halide Perovskites (MHP) have recently gained significant traction as a promising material system due to their excellent properties as a photovoltaic semiconductor as well as low energetic cost of manufacturing. In 2009, when the first perovskite solar cell (PSC) was developed, it had a low efficiency of merely 3.8% [20] which has now improved to a staggering 24.7% as of April 11 2024 [7]. Although, PSCs now rival silicon solar cells in efficiency, they have a major hurdle to overcome. Particularly, they suffer from severe degradation under a variety of environmental conditions such as high temperatures, humidity, oxygen, and ultra violet (UV) radiation [9]. One of the most stable PSCs reported recently boasts 92.9% efficiency retention for up to 1000 hours in ambient conditions at 1 Sun (1000 W/m^2) equivalent irradiation [2]. Comparatively, silicon solar cells maintain their efficiencies for up to 20 years, which is roughly 150 times longer than the state of that art PSCs. Hence, researchers across the world are concentrating their efforts in making MHPs more stable for commercial deployment. There is also a significant push for high-throughput experimentation through automation to expedite research and development in the materials science field. This thesis encompasses advancements in combining these two efforts, aiming to stabilize MHPs and PSCs by incorporating novel

materials and utilizing and developing automated high-throughput research capabilities.

In the following section, a basic introduction to MHPs and PSCs is provided through a discussion of their key structural, chemical, and electronic properties. Additionally, standard characterization methods used throughout this thesis are explained along with guidelines on data interpretation. The second chapter introduces existing automation capabilities, followed by improvements and extensions implemented to further automate and streamline them. In the third chapter, novel materials and chemical additives are investigated as stability and performance enhancers for PSCs. The final chapter concludes the thesis by discussing contributions towards building out an open-source indoor degradation testing platform.

1.3.1 Key Properties of Metal Halide Perovskites and Perovskite Solar Cell Structures

Perovskites were first discovered in 1839 and named after the Russian mineralogist Lev Perovski. The first discovered perovskite mineral was calcium titanate or $CaTiO_3$, but they now represent a class of materials characterized by the chemical formula ABX_3, where A and B represent cations and X represents an anion.

MHPs, a subclass of perovskite materials characterized by organic cations at the A-site, metal cations at the B-site, and halide anions at the X-site, have garnered significant attention owing to their remarkable photovoltaic properties. MHPs have a photoactive alpha (α) phase, characterized by a cubic 3C crystal structure and a photoinactive (δ) phase with 6H hexagonal structure, with undesirable optoelectronic properties. The bandgap of a material signifies the energy difference between its valence and conduction bands, representing the energy threshold required to liberate electrons from the electrostatic forces of the nucleus, allowing for mobility within the material. Thus, an ideal photovoltaic semiconductor would ideally possess a bandgap lower than the energy level of the majority of photons in the solar irradiation spectrum. Hence, the bandgap of these phases is a key determining factor in their photoactivity, where the (α)-phase has a bandgap of around 1.5 eV which is ideal for capturing the irradiation. The (δ)

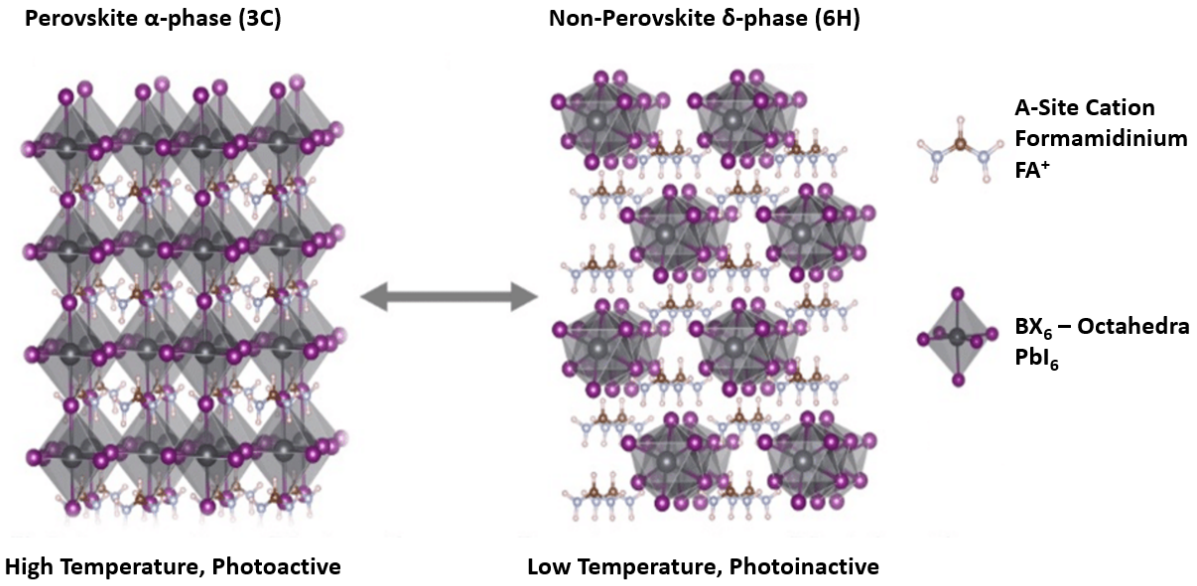

Figure 1.3. Crystal Structures of typical alpha (3C) and delta (6H) phases in MHPs[41]

phase generally has a bandgap higher than 2 eV, which creates too high of an energy barrier to effectively absorb the relatively lower energy photons from the Sun's radiation.

The (α) phase's cubic crystal structure consists of corner-sharing BX_6 octahedra surrounding the larger A-site cation within a cuboctahedral cavity formed by nearest-neighbor X atoms in an AX_{12} polyhedron, Figure 1.3. By varying the composition of A, B, and X ions, the optical and electronic properties of the MHP can be tailored to particular applications. In the MHPs used in high-performance PSCs, lead (Pb_2^+) and iodine (I^-) are commonly used in the B and X sites, respectively. The $[PbI_6]^{4-}$ units feature a Pb 6s–I 5p σ-antibonding orbital as the highest occupied molecular orbital (HOMO). Conversely, the Pb 6p–I 5p π-antibonding and Pb 6p–I 5s σ-antibonding orbitals form the lowest unoccupied molecular orbital (LUMO). This electronic arrangement facilitates a direct bandgap, enhancing the efficacy of charge carrier excitation and recombination processes, unlike silicon, which incurs losses to thermalization. Variations in the A-site cation size primarily affect lattice parameters and octahedral tilting, which also influence the bandgap and other optoelectronic properties of the perovskite.

The ideal compositions of MHPs exhibit several desirable optoelectronic properties due

to their direct bandgap and unique electronic structure [8]:

- Tunable Bandgap: Based on the target application such as indoor photovoltaics or multi-junction solar cells, the bandgap can be adjusted by compositional modifications.
- High Absorption Coefficient: MHPs are able to absorb more light per unit distance compared to traditional silicon. This allows for thinner solar cells, reducing material usage and weight.
- Defect Tolerance: MHPs are less susceptible to the detrimental effects of defects within the crystal lattice. These defects act as shallow trap states rather than deep trap states, minimizing non-radiative recombination and promoting efficient charge separation.
- Long Carrier Lifetime: Due to the defect tolerance, excited charge carriers have a longer lifespan within the material. This allows them to travel further and separate more effectively, ultimately leading to higher photovoltaic efficiency.

PSC architecture comprises of an absorber layer (MHP) sandwiched between an electron transport layer (ETL) and a hole transport layer (HTL), Figure 1.4. The materials for these layers are selected based on their frontier orbital (HOMO-LUMO) alignment with the MHP. Ideally, the conduction band of the ETL should be at the same energy level or lower than that of the MHP, while its valence band should be lower than that of the MHP to prevent holes from entering the HTL. Conversely, the HTL should have energy levels that prevent electrons from entering but allow holes to pass through. Depending on the PSC architecture, one charge transport layer is stacked on a transparent conductive oxide (TCO) such as indium tin oxide (ITO) or fluorine tin oxide (FTO), serving as a charge collecting layer while also allowing light to enter the cell, while the other is stacked with a metallic electrode (e.g., silver, gold, or copper) to complete the solar cell. The choice of architecture (e.g., n-i-p or p-i-n) determines the configuration of these layers and impacts the device's efficiency and fabrication ease. My research focuses on

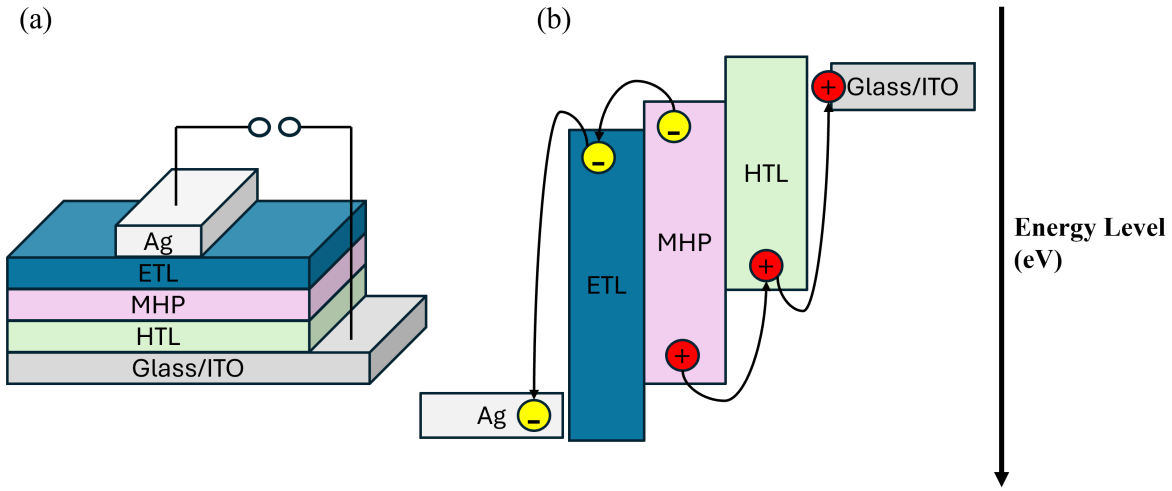

Figure 1.4. a) Architecture of a p-i-n PSC b) Simplified energy level diagram in the PSC

p-i-n PSCs, where the HTL is stacked on top of the TCO, allowing for simplified fabrication and low-temperature processing.

The MHP thin films are generally synthesized using solution processing techniques, with stoichiometrically mixed precursors dissolved in organic solvents. These solutions, also called perovskite inks are coated onto substrates and annealed to lock in the desired crystal phase. The annealing temperature, typically around 150°C , corresponds to the phase transition temperature from hexagonal (δ) to cubic (α) phase. The other layers can be deposited via solution processing or vacuum evaporation methods that are relatively less energy consuming and material intensive to the silicon purification process. Exact recipes used to fabricate MHPs and PSCs will be discussed in more detail in their relevant sections. Some of the key characterisation methods used to test MHP thin films and PSCs will be briefly discussed.

1.3.2 Introducing Key Characterization Methods for Metal Halide Perovskites and Perovskite Solar Cells

Steady-State Photoluminescence

The photoluminescence (PL) of a semiconductor is the emission of light when it absorbs photons of higher energy than it's bandgap. Steady state photoluminescence is the constant

excitation and emission of a semiconductor through an external source of radiation. When the number of emitted photons are normalized for unit time, a curve of photon counts per second (CPS) vs their wavelength or energy can be plotted. This can generally be fit to a Gaussian curve for MHPs, where the peak of the curve roughly corresponds to the bandgap energy of the material, Figure 1.5. The peak of the curve and its full width at half maximum (FWHM) can give an idea of the crystalline quality of the film. A higher peak PL intensity and smaller FWHM are indicators of a low defect density and high crystallinity. Additionally, a slightly shifted peak PL position can indicate defects and trap states in the films which lead to sub-band gap energy states. These can contribute to emission not centered around the bandgap of the MHP. However, there are a few caveats in these conclusions, for example, excess PbI_2 on a films surface can cause surface defect passivation, thereby increasing PL intensity but leading to degradation in the long run [31].

4 - Probe Current - Voltage Characterisation Of Perovskite Solar Cells

The current-voltage (J-V) response of a solar cell under simulated solar spectrum illumination is a standard technique for evaluating device performance. During this measurement, the voltage is swept across a specific range (typically -0.1 V to 1.1 V for PSCs depending on the bandgap) while recording the resulting current response of the solar cell under illumination.

This is generally done with a Source Measuring Unit (SMU) that can be programmed to apply potentials at discrete intervals and measure the resulting current response. Four connections lead out of the SMU, where two probes are used to apply a potential bias across the cell while the other two are used to measure the current response. A typical JV curve is displayed in Figure 1.6

Key Performance Parameters:

- **Open-Circuit Voltage (V_{oc}):** The maximum achievable voltage from a solar cell occurs at the open-circuit point (J = 0).
- **Short-Circuit Current Density (J_{sc}):** The maximum current density a solar cell can

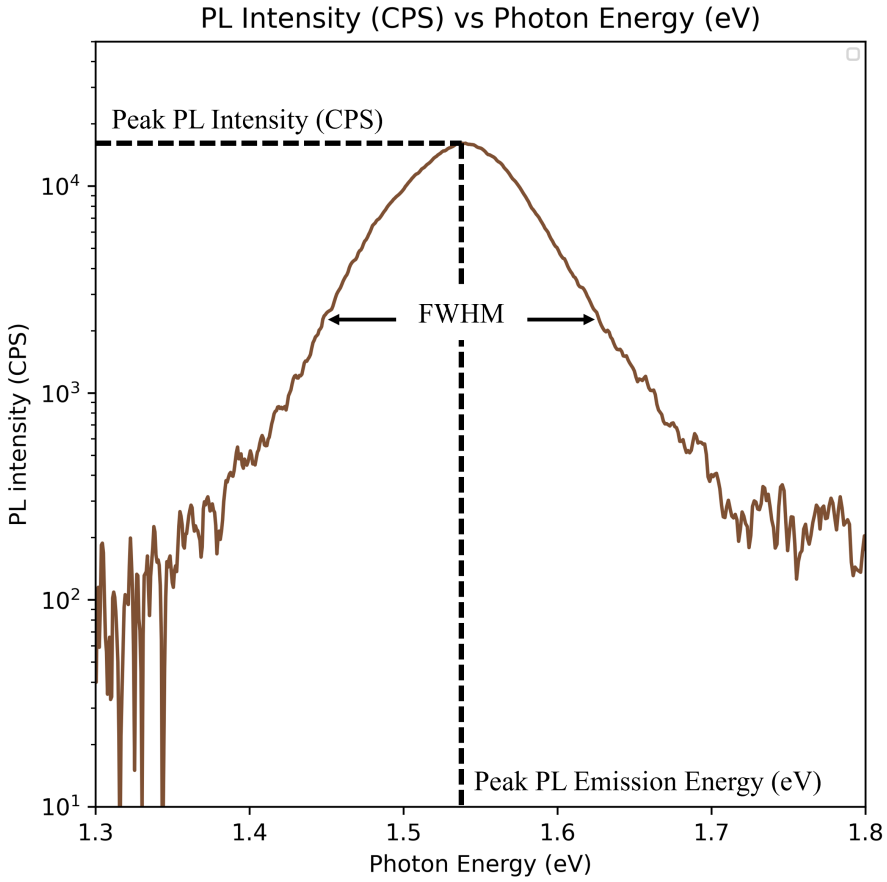

Figure 1.5. Representative PL Spectra of a MHP thin film with a bandgap around 1.53 eV

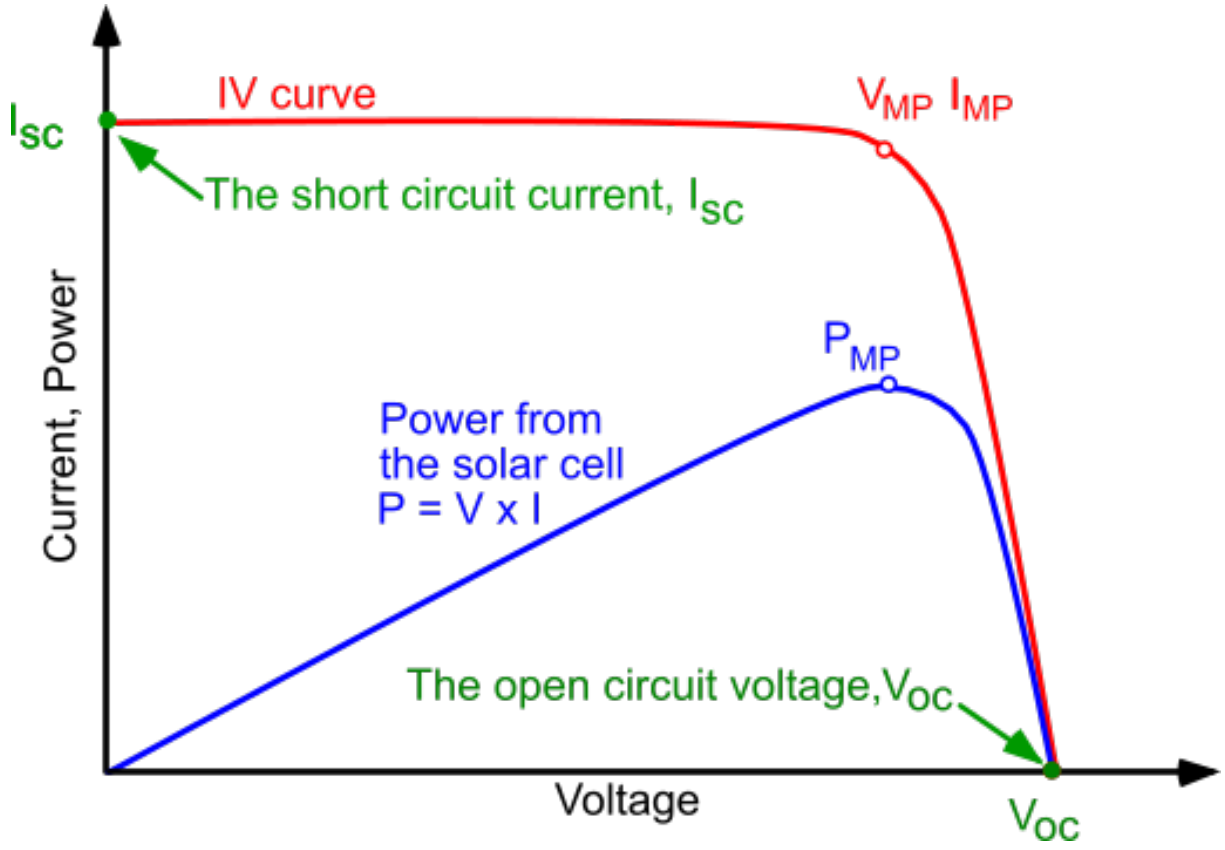

Figure 1.6. Representative IV curve of a solar cell showing key performance metrics [29]

deliver is related to J_{sc}. This parameter is highly dependent on the absorber active layer's optical properties, such as absorption and reflection losses.

- **Fill Factor (FF):** FF reflects how closely a device performs to the ideal case. It is calculated as the ratio of the maximum power point (MPP) to the product of V_{oc} and J_{sc}:

  $FF = (J_{mp} * V_{mp}) / (J_{sc}) * V_{oc})$

- **Power Conversion Efficiency (PCE):** PCE is the ratio of the electrical power output from the device to the incident light power input (P_{in}, typically 1000 W/m²). It is a crucial metric for comparing solar cell efficiencies and is calculated using the equation:

  $PCE = P_{max}/P_{in} = (J_{sc} * V_{oc} * FF) / P_{in}$

Non-Ideal Losses:

- **Shunt Resistance (R_{sh}):** Shunt pathways, often caused by manufacturing defects, allow current leakage within the device, leading to voltage and current losses.

- **Series Resistance (R_s)**: High series resistance signifies an impediment to electron transport, hindering current extraction. These losses can be attributed to energetic barriers at interfaces or bulk resistance within the material. An ideal solar cell would exhibit infinite R_{sh} and zero R_s.

Standard Material Characterizations

Scanning Electron Microscopy (SEM) is employed to investigate the surface morphology of MHP thin films and other transport layers. Current leakage pathways such as pinholes, precipitates on the surface and other artefacts can be revealed as well. Additionally, the average grain sizes, grain boundaries and surface topography can be evaluated to gauge the effectiveness of the MHP in a PSC.

X-Ray Diffraction (XRD) is conducted to verify the crystalline properties of the MHP as well as look for other unwanted crystalline phases in the film such as photoinactive δ phase, PbI_2 and other impurity phases that form due to additives or processing conditions.

Chapter 2

Improving Established Automation Capabilities Of Perovskite Fabrication and Characterization

2.1 Perovskite Solar Cell Fabrication: Process and Challenges

Briefly, The typical fabrication steps for the baseline p-i-n $FAPbI_3$ PSC in the lab are as follows, see Figure 2.1; Glass/ITO stack is purchased from external suppliers which is sonicated in distilled water, acetone and alcohol for 20 minutes each followed by a 20 minute Ultra-Violet Ozone (UVO) treatment. The next step involves spin coating (3000 RPM, 30 s) and annealing (100°C) the HTL, MeO-2Pacz, to form a Self Assembled Monolayer (SAM), followed by spin coating (8000 RPM, 30s) and annealing (150°C) the absorber, $FAPBI_3$. Buckminsterfullerene, also known as C60 is thermally evaporated as the ETL. This is followed by Bathocuproin (BCP) as an interfacial layer to improve energetic alignment on the n-side of the device. Finally, silver (Ag) is evaporated as the metallic contact layer to finish the device. It is well documented that PSC fabrication is incredibly sensitive to processing conditions such as solution dispensing timing, position relative to the substrate, annealing time, etc [35]. Additionally, in the pursuit of high throughput research, a wide and finely controlled sample space is desired, allowing for several discrete conditions in one experiment. The endurance and skill of human operators is a

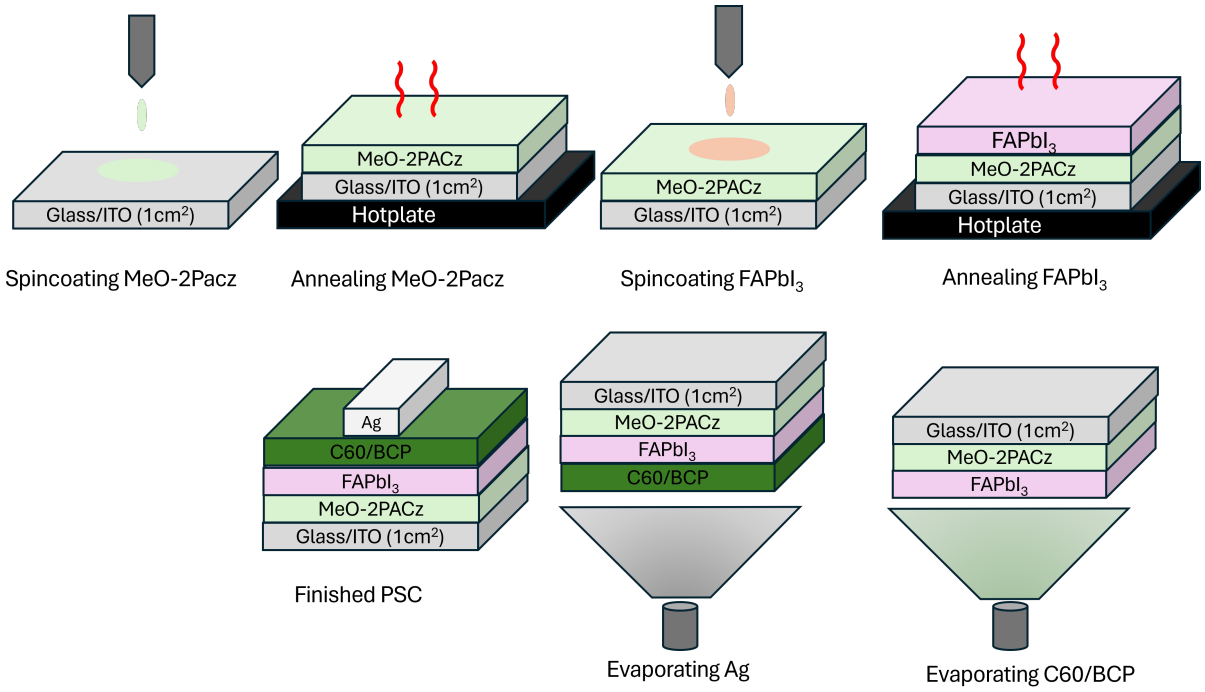

Figure 2.1. Schematic of the baseline p-i-n PSC fabrication process

limiting factor in this endeavour.

Hence, The Perovskite Automated Spin Coat Assembly Line (PASCAL), a novel platform was developed by graduate students at SOLEIL to streamline experimentation by automating various stages of the conventional PSC thin film fabrication process [3]. PASCAL's functions include liquid handling, spin coating, annealing, and thin film characterization using techniques like PL imaging and PL spectroscopy. Its six main components highlighted in Figure 2.2 include a liquid handler (Opentrons OT2) for precise solution mixing and dispensing, a custom spin coater, three hotplates for annealing and thermal degradation assessments, a characterization train for PL imaging and spectroscopy, two substrate storage trays (45 10 mm x 10 mm substrates per tray), and a gantry with a gripper for sample transfer. The custom spin coater fits into one of the liquid handler's deck slots for direct solution dispensation. To preserve sample integrity, PASCAL operates within a nitrogen glovebox to maintain oxygen and water levels below 1 ppm, crucial for PSCs sensitivity to humidity and oxygen.

After the half cells are fabricated and characterised in PASCAL, they are manually

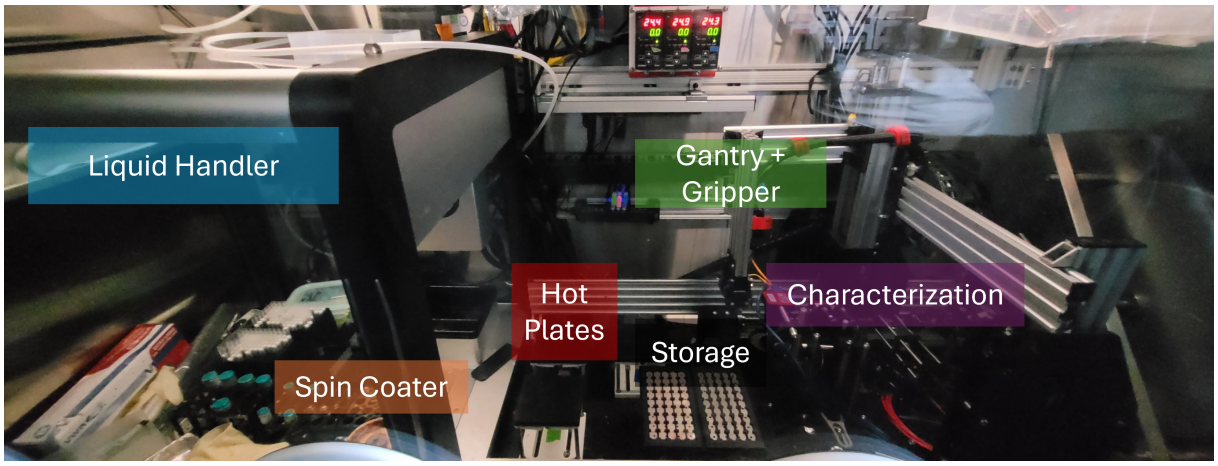

Figure 2.2. An image of PASCAL highlighting its main components

transferred in an air-free container to the Physical Vapor Deposition (PVD) chamber where the devices are complete with ETL and metallic contact deposition. After device fabrication is completed, the cells are tested inside a nitrogen environment with 4 probe JV testing as mentioned previously.

Although the thermal evaporation process does not involve operator handling, all the transfer processes require physical human intervention. This proves to be a limiting factor as well. The surface of PSCs are particularly vulnerable due to the presence of soft materials such as the organic C60/BCP ETL and the organic-inorganic MHP. Even minor contact with sharp tweezers can cause surface abrasions, resulting in device shorting. Moreover, the combination of small substrate sizes (10 mm) and the use of thick butyl rubber gloves in the glovebox exacerbates the challenge of handling PSCs. Additionally, a minor slip when making contact with the microprobes generally used in JV testing can permanently damage the PSC. In a batch of 45, JV testing typically takes 3 to 4 hours, with 4 to 5 PSCs inevitably damaged by operators. Consequently, there arose an urgent need to introduce an automated JV testing setup to meet the demands of high-throughput research enabled by PASCAL.

2.1.1 JVBot: Automated Current-Voltage Testing of Perovskite Solar Cells

I developed the JVBot to automate the JV testing of PSCs fabricated by PASCAL. It has the capability to automatically test a batch of 45 PSCs within an hour, with an additional 15 minutes required for setup time, achieving near 100% accuracy without causing any damage. The JVBot's design mirrors that of a Fused Deposition Modelling (FDM) 3D printer, featuring a rectilinear gantry controlling a mobile bed. The bed accommodates a removable tray with 45 slots for the PSCs, each with holes serving as individual aperture masks, with an area of 0.07 cm^2. In contrast to an FDM 3D printer's filament extruding nozzle, the JVBot is equipped with a probehead housing 4 spring-loaded probes, known as pogopins, for contacting the PSCs. The JVBot is constructed as a mobile unit supported by 4 standoffs, facilitating easy movement and storage within the glovebox.

The JVBot's frame is constructed using metric T-slot extrusions, with stepper motors on the X and Y axes facilitating movement around the bed via a belt and pulley system. The bed comprises a custom-designed and machined aluminum tray holder attached to the frame via rubber wheels mounted on a wheel plate, enabling movement in the XY plane as the stepper motors pull the belt fastened to the wheel plate. A stepper motor drives a leadscrew stage attached to a beam running through the center of the X-axis and parallel to the Y-axis, allowing the probehead to traverse the Z-axis with precision. This mechanical system, referred to as the gantry, is controlled by an SKR Mini E3 control board utilizing open-source Marlin Firmware specifically tailored for 3D printers. Figure 2.3 is an image of the JVBot in the glovebox with its main components highlighted.

To initiate a testing sequence, the JVBot is positioned above a window on the glovebox floor, as depicted in the figure. A solar simulator, housing a filtered Xe short-arc lamp beneath the glovebox, provides irradiation for the PSCs. The light intensity is calibrated using a KG5 silicon reference cell positioned at the same elevation as the PSCs in their trays. The bed is

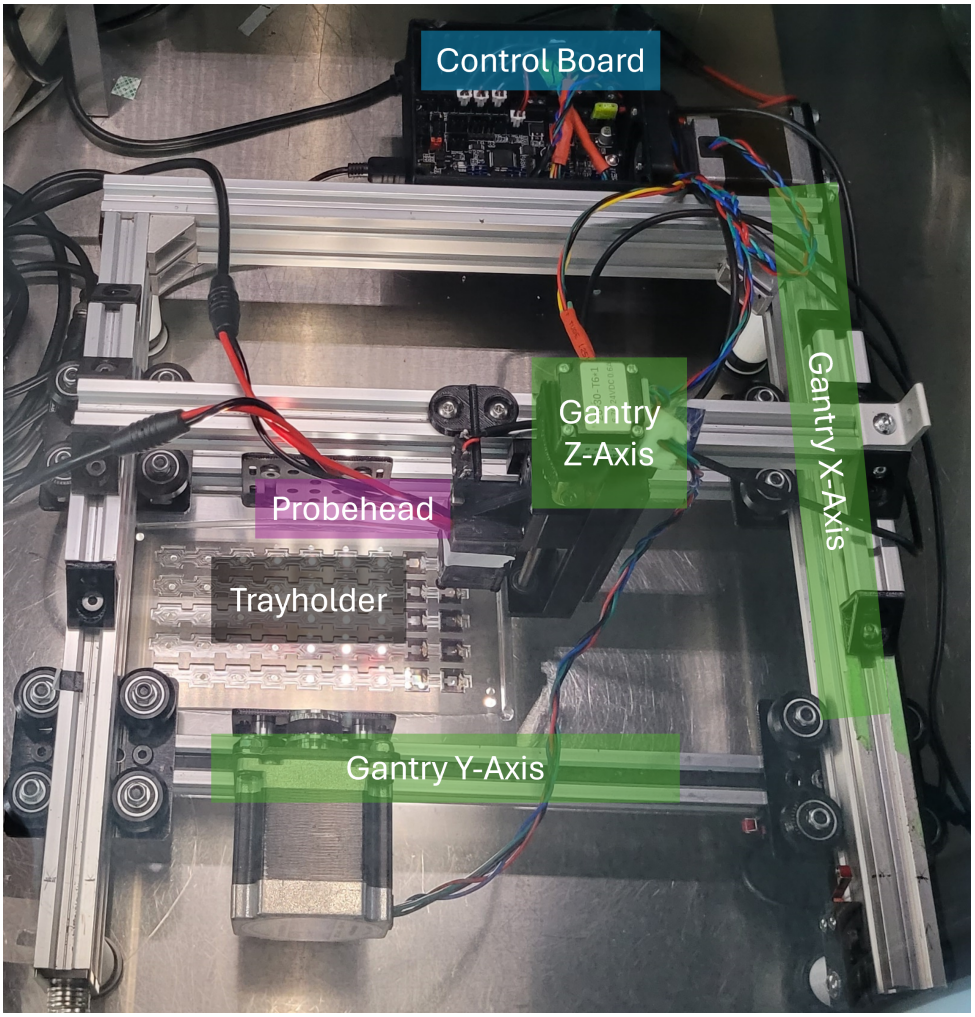

Figure 2.3. An image of JVBot highlighting its main components

then loaded with the PSCs, oriented such that the metallic contact layer faces upwards towards the probes. Subsequently, the bed positions each PSC directly beneath the probehead, which descends slowly along the Z-axis. Upon contact, the pogopins are further depressed to load their springs, exerting firm pressure on the PSC. Two pogopins make contact with the metallic layer, while the other two pierce through the device layers to the TCO, completing the device circuit. The probehead connects to a Keithley SMU situated outside the glovebox via BNC cables. A custom Python script controls the Keithley, executing a pre-programmed JV sweep. The integration of mechanical and electrical control is consolidated within the JVBot Python program, available as open-source on the Fenning Research Group Github.

2.2 Further Optimizing Perovskite Fabrication and Characterisation Process

Despite the film fabrication and characterisation itself being completely automated and hands free through PASCAL, there are several steps before and after that still require operator handling. The schematic in Figure 2.4 (a) shows the entire fabrication to degradation testing process highlighting steps with human intervention and time involved in each step.

10 mm x 10 mm ITO coated glass substrates are taken out of their boxes and placed vertically in cleaning racks. After the cleaning steps (40 min), they are placed on a metal tray for UVO treatment (20 min). The substrates are then individually transferred using tweezers into the PASCAL tray which is then brought into the glovebox through a small antechamber (7 min). The UVO treatment is time-sensitive, requiring immediate initiation of deposition afterward. Furthermore, the ultra-clean substrate surfaces are highly susceptible to contamination. Therefore, manual substrate transfer by an operator results in both a loss of valuable time and a high risk of contaminating the substrate surface. Previously, PASCAL trays consisted of two layers: an aluminum base plate and a plastic slot layer. However, the plastic layer would degrade under UVO treatment, rendering it unsuitable for immediate use after the washing step.

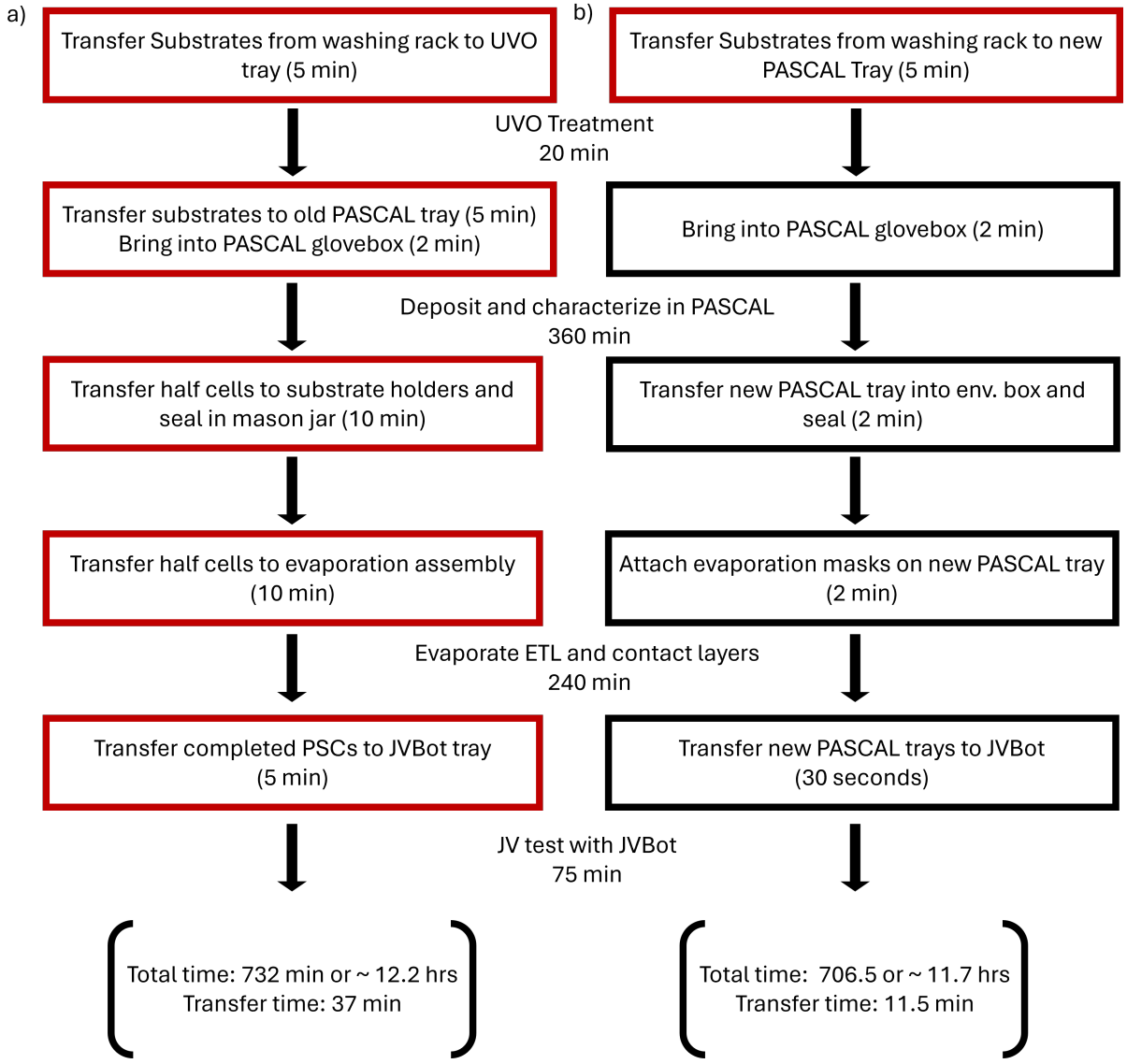

Figure 2.4. PSC fabrication process with a) old PASCAL trays and b) new PASCAL trays. Steps involving operator handling of substrates highlighted in red boxes

After the tray is placed in PASCAL and the deposition and characterization are completed (360 min for 45 substrates), half-cells—referring to partially completed PSCs—are transferred into 2-inch x 2-inch plastic containers with 3D-printed inserts to hold substrates (10 min). Each container can accommodate 16 half-cells, necessitating the use of 3 containers to hold an entire batch of PASCAL-fabricated half-cells. Once again, the half-cells, comprising incredibly fragile thin films, need to be transferred one by one by an operator in the glovebox, often resulting in surface damage due to mishandling. Subsequently, the substrate holders are sealed in an airtight mason jar to be transferred to another glovebox for PVD and JV testing.

Once the half cells are taken into the glovebox with the PVD chamber, they are transferred to a 3 layer, laser cut mask for PVD (10 min). The bottom layer acts as a base plate to hold the substrate while the middle layer has slots which hold them in place. The top most layer acts as the evaporation mask with the slot shape corresponding to the layer being deposited i.e ETL or metallic contact. The half cells are then transferred manually by an operator to the first two layers of the mask and followed by putting on the final layer of the mask. This step needs to be executed with utmost caution due to the fragile nature of the soft thin film layers where any damage to the surface can lead to shorting of the device, rendering it useless. Once the PSCs are complete in the PVD chamber (240 min), the top layer of the mask is disassembled and the substrates are transferred by hand to the tray of the JVBot (5 min). This again must be performed with utmost caution due to the fragility of the complete PSC. The JVBot then JV tests the devices after which they are taken for degradation testing which will be discussed further in chapter 4.

Clearly, there were several operating procedures in the past that limited the productivity of the automated fabrication and characterization process. Hence, there was an urgent need to address these bottlenecks. The ideal situation to streamline this process would be to have a single tray into which the substrates could be placed after the washing step and only removed after JV testing. The limiting factor here was the tolerances in the slot width of the tray.

The original tray used in PASCAL has a slot width of 10.9 mm while the substrate size was around 10.1 mm. This 0.8 mm gap allowed the substrates to move around in the tray, leading

to the following issues:

- The substrates had to be centered in the slot with tweezers right before depositions to ensure successful pickup by PASCAL's gripper. Any misalignment leads to the tilting in the grippers teeth leading it to drop the substrate.
- Because the half cells can move around in the tray, the evaporation mask would not perfectly align with the etched ITO tab, potentially leading to shorts as the contact deposits over the ITO surface of the half cell.
- The pogopins of the JVBot could not be accurately calibrated to contact the small 3mm metallic tab and ITO in an entire tray due to the unpredictable position of the PSCs. Consequently, the pogopins might make contact with the wrong surface or entirely miss the PSC and contact the surface of the tray.

In an attempt to fix this issue, the tolerances of the slots in the tray were tightened. Upon tightening the slot width of the PASCAL tray to 10.4 mm which is an acceptable tolerance for the evaporation mask and JVBot tray, PASCAL's gripper failed to pick up substrates. Even the slightest tilt in the substrate, which is unavoidable, led to the substrate walls making contact with the slots of the tray. The frictional forces as a result of this contact fought against the vertical movement of the gripper as it pulled the substrate out of the tray. This led to severe tilting of the substrate in the grippers teeth, eventually causing the substrate to fall out of its grip.

I devised a solution for this using chamfered trays, essentially slanting the walls outwards from the bottom up. This enables the use of a tighter tolerance at the bottom of the slots while also eliminating most of the glass to slot wall contact. Hence, a combination of bottom slot widths and chamfer angles were experimented with to find the tightest tolerance the gripper could handle. Summarizing this effort, slot widths of 10.6 mm and higher led to significant substrate disorientation while 10.2 mm wouldn't completely accommodate the substrates. Changing the chamfer angle had no effect on the tighter slot widths. Finally, a bottom slot width of 10.4 mm

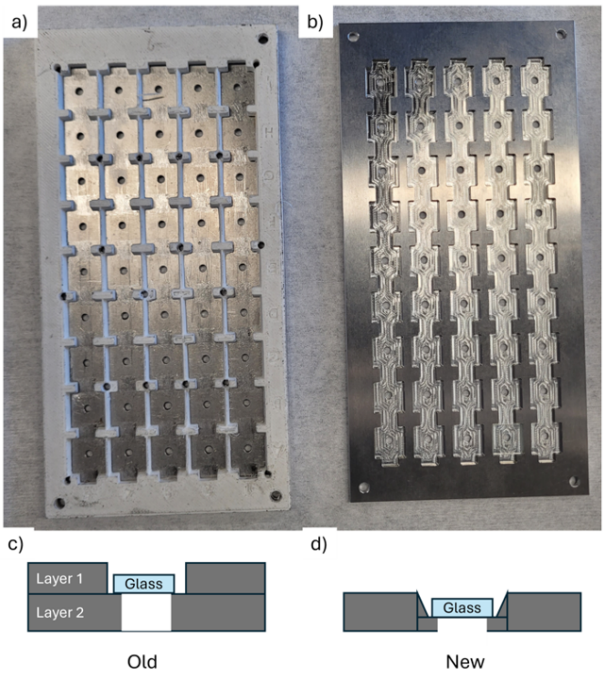

Figure 2.5. Image and cross sectional schematic of a),c) old PASCAL tray and b),d) new PASCAL tray

along with the a chamfer angle of 80°Θ was found to be optimal, accommodating the substrate and preventing significant glass to slot wall contact.

The new PASCAL trays as seen in Figure 2.5, each containing 45 slots, were manufactured from aluminum as single pieces, featuring chamfered slots and a thin bottom layer measuring 0.6 mm, with 0.07 cm^2 aperture holes designed for JV testing. The entire tray has a thickness of 2 mm, with 1.4 mm allocated for slot height. PASCAL's storage component accommodates two such trays, allowing for the fabrication of 90 PSCs in a single experiment. Previously, only one tray was used due to significant challenges during the PSC fabrication process. These challenges discouraged attempts to increase sample production due to the time-consuming nature of the process and the risk of losing many PSCs. However, the introduction of these new trays facilitated process improvements, along with some hardware changes, as depicted in the schematic in Fig 2.4(b).

1. The washed substrates are transferred directly to the aluminum PASCAL trays (5 min),

which are then placed into the UVO machine.

2. Upon completion of UVO treatment, the trays are directly transferred into PASCAL (2 min), and deposition can begin immediately.

3. After PL characterization, the trays are transferred into an environmentally sealed aluminum box (2 min). The box is vacuum-sealed and transported to the glovebox holding the PVD chamber.

4. The trays are removed from the box and positioned on a 3D-printed jig for easy assembly of the evaporation stack. The evaporation masks are screwed directly on top of the two trays; each mask can hold two trays (2 min). There is also the option of using a smaller mask for one tray. The short wall height and 80°Θ chamfer angle significantly restrict sample mobility as the evaporation assembly is flipped over for deposition. This ensures that the mask and 1.1 mm thick substrates are perfectly aligned.

5. After the PVD steps, the mask is unscrewed, and the trays are placed one at a time in the JVBot (30 seconds). Currently, the JVBot can only accommodate one tray per test due to dimensional constraints in the glovebox. Plans are in place to procure a larger glovebox in the future, allowing for testing of two trays simultaneously.

Following JV testing, devices can either be transferred by hand from the tray to sample holders for storage, or the entire tray can be inverted to discard the devices. The trays are then ready for reuse in subsequent experiments. With the new PASCAL trays, the transfer time is reduced from 37 minutes to 11.5 minutes, a 69% decrease. Additionally, the risk of damaging samples during transfers has been significantly reduced by minimizing human intervention wherever possible.

Chapter 3

Effort Towards Improving Perovskite Stability and Performance Through Substitution, Additives and Stack Engineering

3.1 B Site Substitution of Barium in $FAPbI_3$ to Improve Stability via Goldschmidt Tolerance Factor Tuning

Introduction

Tuning the Goldschmidt tolerance factor (GTF) is one of the most popular ways to improve the stability of MHPs [23]. It is an empirical metric that predicts assesses how well the A-site cation fits within the BX_6 octahedra in the perovskite structure. The expression for the tolerance factor (t) is as follows:

$$t = \frac{r_A + r_X}{\sqrt{2}(r_B + r_X)}$$

Here r_A, r_X and r_B are the radius of the A-site, X-site and B-site ions respectively. A tolerance factor of 0.9-1 generally leads to a cubic phase which is the photoactive α phase while going higher than that leads to a tetragonal phase and lower than that leads to an orthorhombic phase. Hence, in general it is favorable to keep the MHP in the cubic phase. Accordingly, several studies have been done to on ionic substitution to modify the GTF to more favorable values. However, most of these studies that are successful are on A-site cations because of its

body centered position in the lattice. The BX_6 octahedra can tilt to accommodate different size ions and hence there is more flexibility in choice of cation. Additionally, A-site cations do not contribute much to the electronic structure of the perovskite as discussed in the introduction. X-site substitution is generally to tune the bandgap of the perovskite due to their electronic contribution to the BX_6 octahedra, however looking at the GTF expression, their structural contribution is minimal compared to the A and B site.

The role of the B-site is peculiar in the regard because it plays both a structural and electronic role in MHP system. The size of the B-site cation can affect the size of the octahedra as well as change the electronic structure of the MHP leading to changes in bandgap amongst other properties. Tin (Sn) is one of the most widely studied B-site subtituent as a means to reduce toxic lead in MHP as well as widen the bandgap for tandem applications [25].

Other cations such as Sr, Ge, Cu, Hg, etc have also been studied several years ago but interest in this endeavour dwindled due to only marginal gains in PSC performance[11] [4] [21]. This is mainly because the B-site substitution lead to only minor morphological gains in MHP thin film due to solvent-ion complexes that improved crystallization dynamics. Viz. they contributed little to the MHP lattice and electronic structure.

However, in further pursuit of verifying the effects of B-site substitution in MHP, I conducted a case study on the effect of barium (Ba) substitution in the $FAPbI_3$ system. B-site Ba substitution has been investigated in $MAPbI_3$ as well as inorganic $CsPbIBr_2$ with varying degrees of success [33][5]. However, the exact role Ba plays in improving the crystallinity and morphology MHP thin films is still not clear.

Ba^{2+} has an ionic radius of 135 ppm while lead has an ionic radius of 119 ppm. The larger size of Ba^{2+} makes it an ideal candidate for partial B-site substitution of Pb^{2+} in $FAPbI_3$ as it can bring down its GTF which is around 1, making it more stable according to the GTF rule. It is hypothesized that incorporating a small amount of Ba $< 5\%$ could lead to the formation of a more stable and high crystallinity MHP film. Hence, in this study attempts are made to incorporate Ba in $FAPbI_3$ and fabricate thin films, followed by characterizing their crystalline,

morphological, and electronic properties, as well as testing their stability. Through various attempts of process engineering, compositional tuning and single-crystal growth, it is founnd that Ba^{2+} is incompatible with the formation of BX_6 octahedra in $FAPbI_3$ due to its electronic structure lacking np2 lone pair electrons, likely inhibiting the formation of cubic perovskite phase as well as a lack of ideal optoelectronic properties.

Initial Attempts and Developing a New Recipe

Another graduate student in our lab was briefly working on this project before it was passed on to me. In an initial attempt to incorporate Ba in $FAPbI_3$ they synthesized $FAPb_{(1-x)}Ba_{(x)}I_3$ (x = 0.025, 0.05, 0.01, 0.2, 0.3), varying the % Ba substitution from 2.5 to 30%. Here the lab standard recipe was used; 1.3 M $FAPbI_3$ dissolved in 2 Methoxyethanol (2ME) with 0.2 M Methylammonium chloride (MACl) as an additive and 7.5% by volume N-Methylpyrrolidone (NMP) as the coordinating non-volatile solvent. Looking at the pictures and SEM images of the Ba incorporated $FAPbI_3$ films in Figure 3.1. It is observed that 2.5% Ba incorporated films looked visually standard but revealed what could possibly be Ba or Ba compound precipitates scattered on the surface. At higher % of incorporation a reddish tint is observed, indicating a non-cubic perovskite phase. Upon taking over this project, I decided to develop a recipe using more coordinating solvents which requires the use of an antisolvent (AS). This is in pursuit of fully dissolving Ba in the solution and successfully incorporating it in thin films via spin coating.

Upon performing a literature survey of commonly used solution formulations and processing conditions, a 4:1 by volume DMF:DMSO (Dimethylformamide:Dimethyl sulfoxide) solvent mixture and chlorobenzene AS was chosen. The recipe was further developed to tune the molarity of $FAPbI_3$ and AS drop timing. iPACl was chosen as an additive due to its solution stability and high crystallinity promoting properties in $FAPbI_3$ [28]. The iPACl molarity was optimized to 0.3M, giving the strongest 14°2Θ peaks which corresponds to the (100) plane in α $FAPbI_3$. Along with this, it was ensured that there were no impurity phases in the film. The final

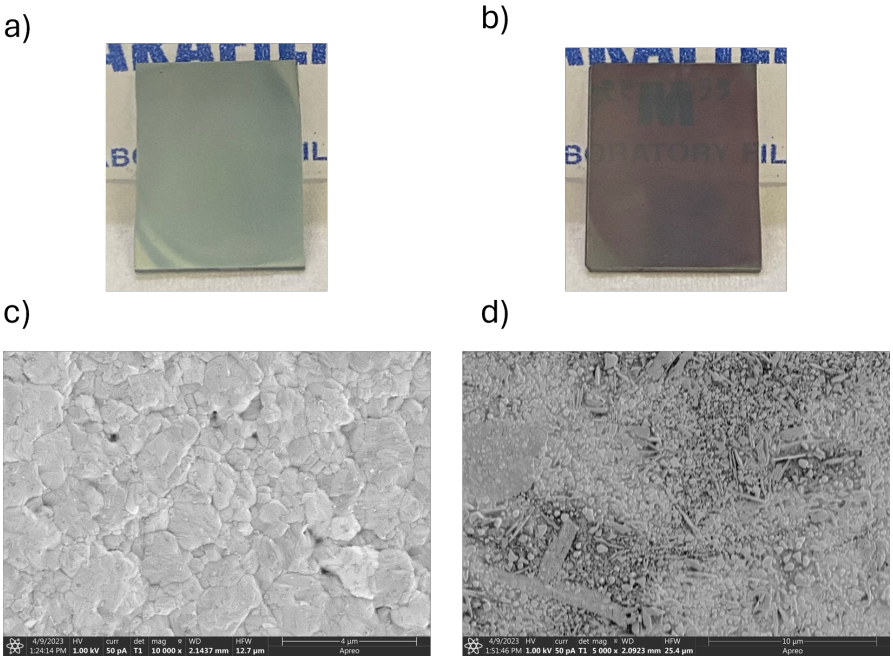

Figure 3.1. Pictures of a) Ba 2.5% b) Ba 5% films and SEM images of c) Ba 2.5% d) Ba 5% films

recipe was as follows; 2M $FAPbI_3$ with 0.3M iPACl in 4:1 DMF:DMSO solution spin coated at 6000 RPM for 35 seconds with an AS drop time of 31 seconds. The films are annealed for 10 minutes at 150°C.

Incorporating Barium at Logarithmically Scaled Amounts

With an established recipe for $FAPbI_3$ using a highly coordinating solution, optimised AS drop time and additive molarity, the incorporation limit of Ba in the B site of $FAPbI_3$ was probed. This was started off with a logarithmic scaling of Ba substitution of 0.1, 1, 10% in the B site of $FAPbI_3$. Films were spin coated on glass/Me-O2Pacz and characterized with PASCAL's steady state PL setup.

Looking at the PL in Figure 3.2 a) and b), the control condition with 0% Ba, the maximum intensity of PL is around 10^5 CPS and the peak position with very little deviation. However, with incorporating even 0. 1% Ba there is significant variability in PL ranging from 0.5×10^5 to 10^2 CPS. The Ba 1% condition shows peak PL intensities around 10^4 CPS which is an entire

magnitude lower than the control. The 10% Ba shows peak PL centered around 10^2 CPS and a slightly higher peak PL intensity likely due to defects affecting the energy levels of the perovskite. Additionally, SEM images of the films were taken. Figure 3.2 c), revealed dense coverage of the 10% Ba film with what are likely to be BaI_2 precipitates. This would explain the tight distribution of the peak PL intensity of 10% Ba films due to surface passivating effects. However, these results are inconclusive in determining the successful incorporation of Ba in the $FAPbI_3$ lattice. It is likely the energy barrier for Ba incorporating in the BX_6 octahedra is much higher than for Pb. Hence, in attempt to make Ba incorporation more favorable an excess amount of Ba is introduced in the solution to potentially drive in the Ba^{2+} cation into the lattice.

Hence, Ba is again logarithmically scaled in excess in the $FAPbI_3$ solution as $FAPbBa_{(x)}I_{3+2x}$ Films synthesized with same solution and processing conditions. Looking at the PL in Figure 3.3 a) and b), significant variation of peak PL in the control condition is observed, likely due to some solution aging or improper deposition, however, a tight distribution of peak PL energy is seen, indicating successful formation of cubic $FAPbI_3$. An exponential decay in the peak PL intensities of the films from 0 to 10% Ba with the Ba conditions showing a peak PL intensity of around 10^2 CPS is observed. This is almost 3 orders of magnitude lower than that of the control, indicating very poor crystallinity in the films. There is also a 0.15 eV increae in peak eV of the 10% Ba films which is further elucidated by the SEM images, Figure 3.3 c) and d). The SEM images of the Ba 10% reveal dense coverage of a BaI_2 film on the surface which likely led to this increase in peak energy. Additionally, the 1% Ba condition shows BaI_2 precipitates distributed on the surface of the film which also explains the tighter PL intensity distribution of this condition.

In previous attempts in literature on B-site doping, generally with $MAPbI_3$, the divalent cation added to the MHP solution led to smoother morphology as well as higher crystallinity, showing little evidence of actual lattice incorporation. Hence, it is theorized that the BaI_2 added to our solution may be competing with the iPACl in its role as an additive and vice versa. Hence, in an attempt to decouple this interaction Ba substituted $FAPbI_3$ films are fabricated with the original recipe, scaling it logarithmically as in the initial batch. For each condition of Barium,

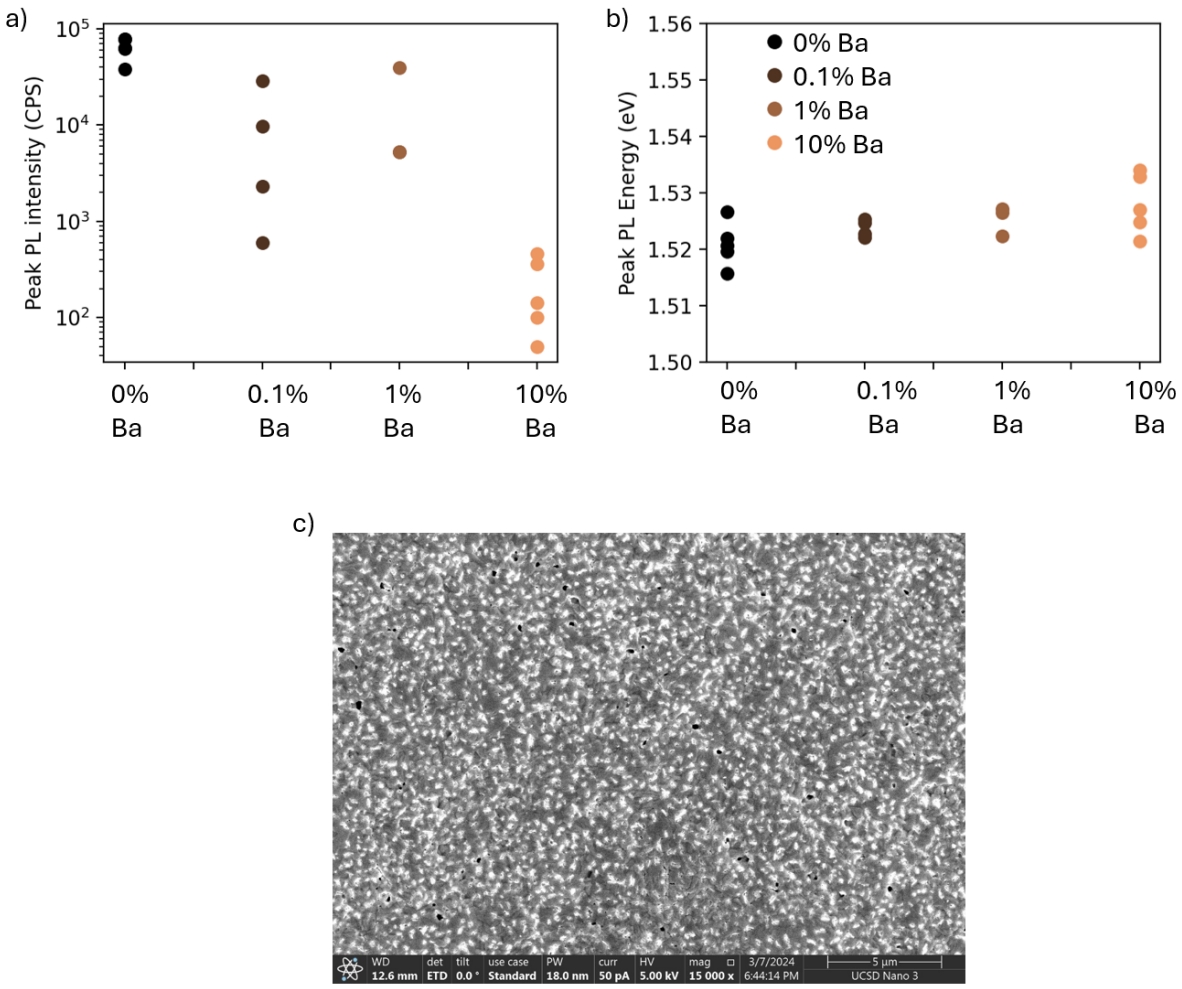

Figure 3.2. Peak PL a) Intensity and b) Energy of the barium substituted $FAPbI_3$ films. c) SEM Image of 10% Ba substituted $FAPbI_3$ film

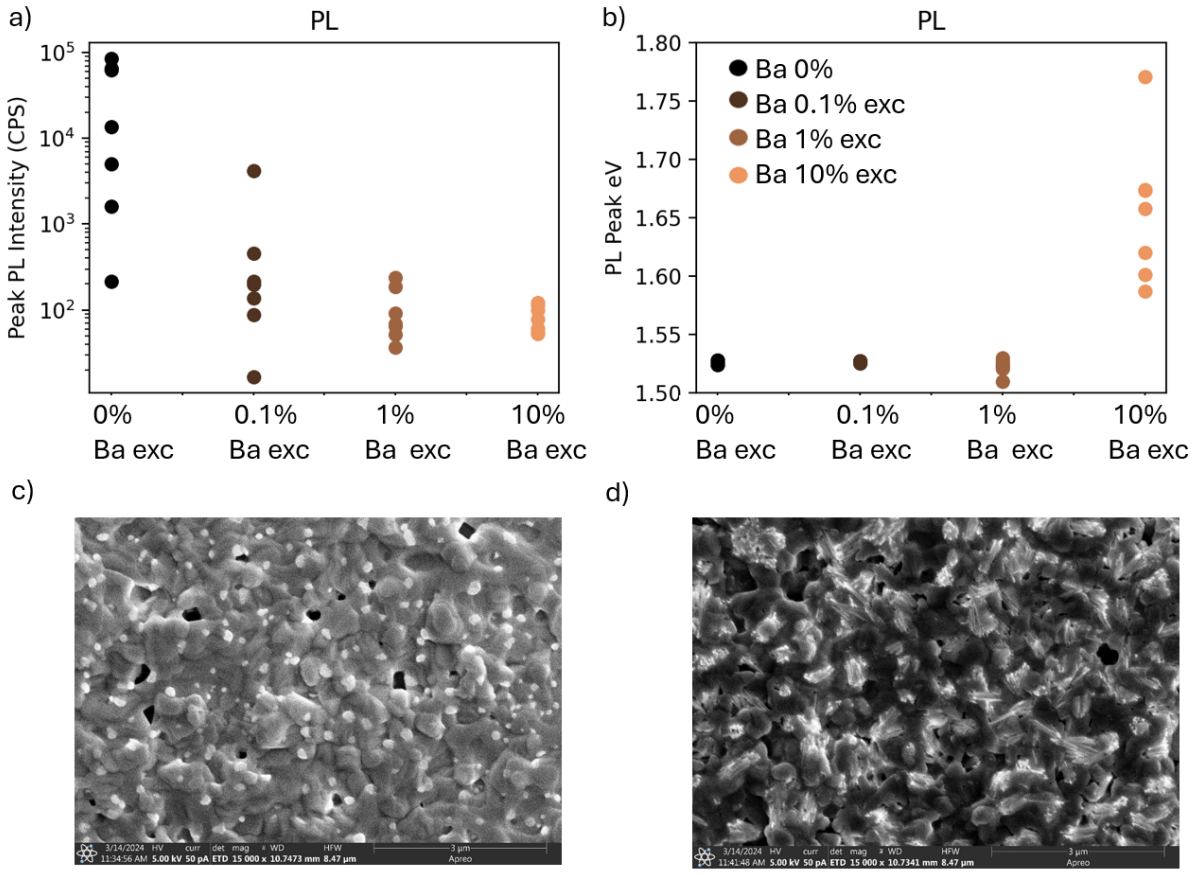

Figure 3.3. Peak PL a) Intensity and b) Energy of the excess barium incorporated $FAPbI_3$ films. SEM Image of c) 1% and d) 10% excess Ba substituted $FAPbI_3$ film

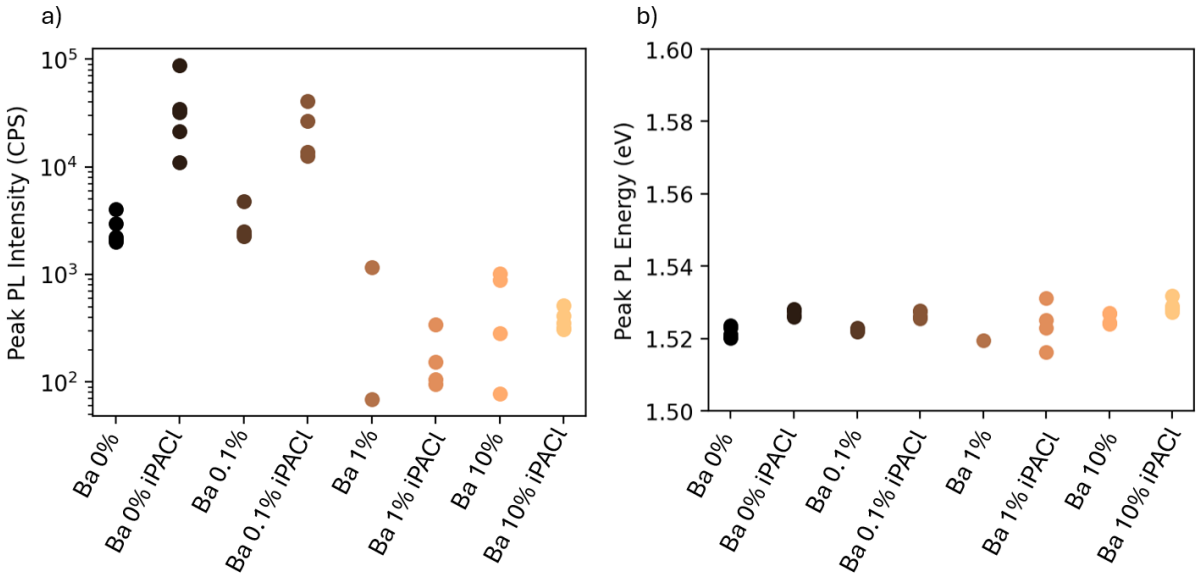

Figure 3.4. Peak PL a) Intensity and b) Energy of Ba substituted $FAPbI_3$ with and without iPACl

films with and and without the iPACl additives are made.

Looking at the peak PL intensities of these films in Figure 3.4, the 0% barium condition with iPACl has an average PL intensity of 0.5×10^5, slightly lower than previous batches, however, it is an entire order of magnitude higher than the without iPACl condition. Similar trends for the 0.1% condition. Comparing the 1% condition with and without iPACl, the average PL is more or less the same, however, there is a an anomalous, order of magnitude of deviation between the two recorded films. The 10% Ba without iPACl condition shows great variability again but is centered around 0.5×10^5 CPS while the 10% iPACl shows a tight distribution around the same PL value. However, in general, replacing iPACl with BaI_2 as a potential additive seems to have no beneficial effect, as the control with iPACl far outperforms the other conditions.

Stability Testing of Ba incorporated $FAPbI_3$ films

An ISOS-L2 test was conducted on these films using our home built system, maintaining a constant N_2 environment, 75°C surface temperature and 1 Sun illumination from LED grow lights [17]. A picture of the films is taken every 30 minutes for around 700 hours and the change in color is tracked on each film based on Hortana et al's work [16]. The films start out greyish

black and over the course of the experiment begin to turn yellow, changing from α to δ phase over the course of the experiment.

The RGB pixel values in each image were transformed into the CMYK color scale. Subsequently, the grayscale component (K) within this color scale was utilized as a representative indicator to quantify the transition from α phase to the photo-inactive δ yellow phase. The mean K value of the pixels in each film was tracked as a function of time. The environmental box used to hold the films was bumped a few times throughout the experiment which manifests as sudden changes in mean k value, happening around 200, 300, 450 and 620 hours. However, it is most important to examine natural/gradual change in mean K value. Looking at Figure 3.5, the films with iPACl show initial burn-in phase where in the first 100 hours where the K value drops in the first 10 hours and gradual increases to a stable value. The onset of degradation is marked when the mean K value shows a consistent drop in value and is signified as t_{deg}. The Ba 10% film begins degrading first as its mean K value starts around 151 hours initially showing a slower rate of change but quickly increasing at around 250 hours. Ba 10% with iPACl begins degrading around 205 hours with a more sharp onset of degradation. The Ba 1% conditions show a similar trend where the without iPACl conditions begins degrading sooner but in a more gradual nature at 216 hours. The Ba 1% iPACl condition sees an onset of degradation around 410 hours as a steeper curve. Interestingly, sub 1% Ba films have a reverse nature where the without iPACl conditions are more stable, with Ba 0% proving to be the most stable film tested. It's degradation onset occurs at 621 hours while the Ba 0% with iPACl condition begins changing phase in about half the time at 332 hours. The Ba 0.1% without iPACl condition shows an onset of degradation at 506 hours while Ba 0.1% begins to phase change at 303 hours.

These results are summarized in Figure 3.6. Surprisingly, Ba 0% has the highest stability followed by Ba 0.1% and Ba 1% iPACl. The trend in sub 1% substituted Ba $FAPbI_3$ is that the iPACl conditions tend to have lower stability than their without iPACl counterparts. This is likely due to the leftover iPA deprotonating FA^+ cations at elevated temperatures leading to film degradation. This phenomenon will be further discussed in coming section. On the other

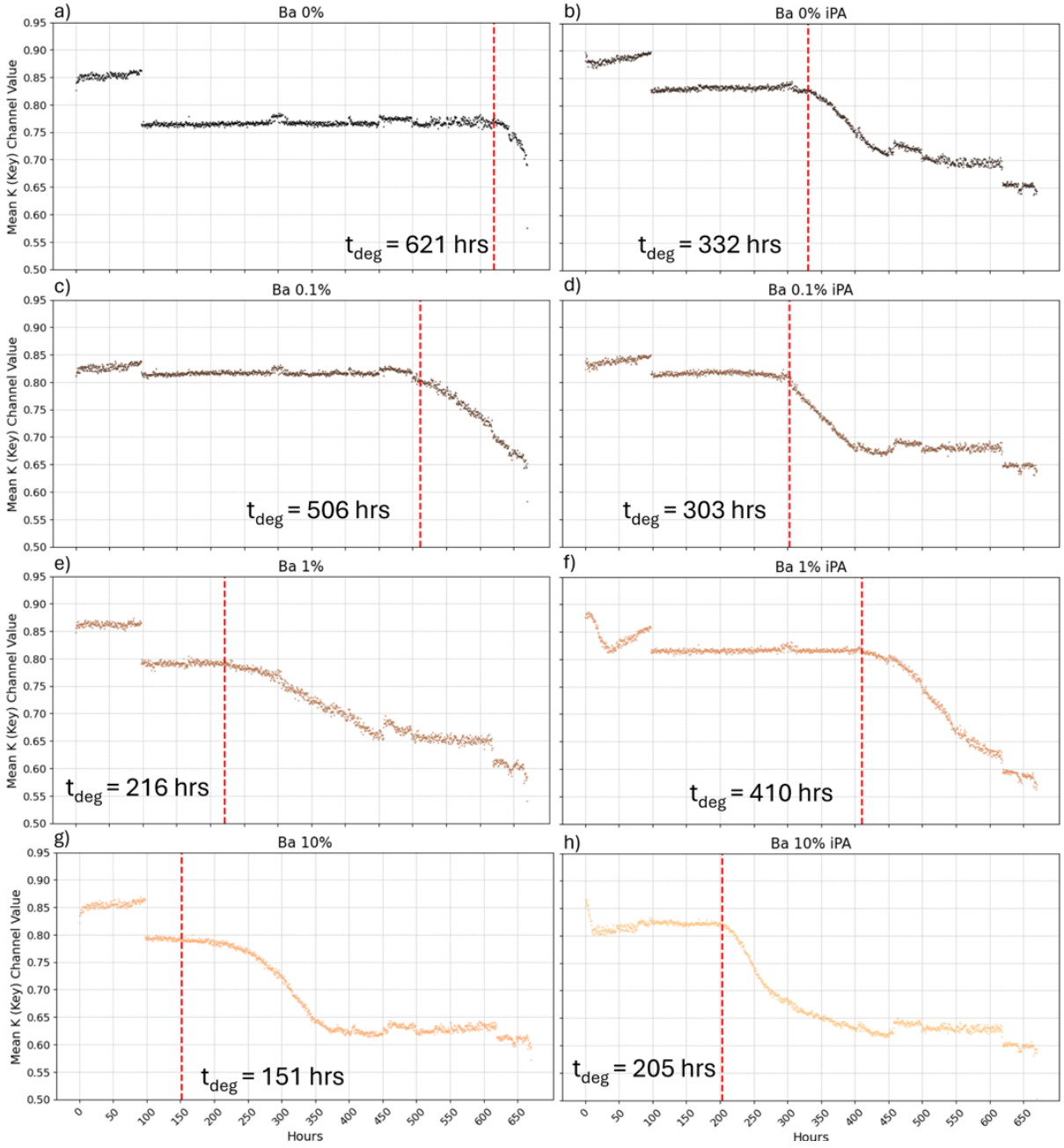

Figure 3.5. Mean K value in as a function of time in hours in a) 0% Ba b) 0% Ba with iPACl c) 0.1% Ba d) 0.1% Ba with iPACl e) 1% Ba f) 1% Ba with iPACl g) 10% Ba g) 0% Ba with iPACl $FAPbI_3$ films

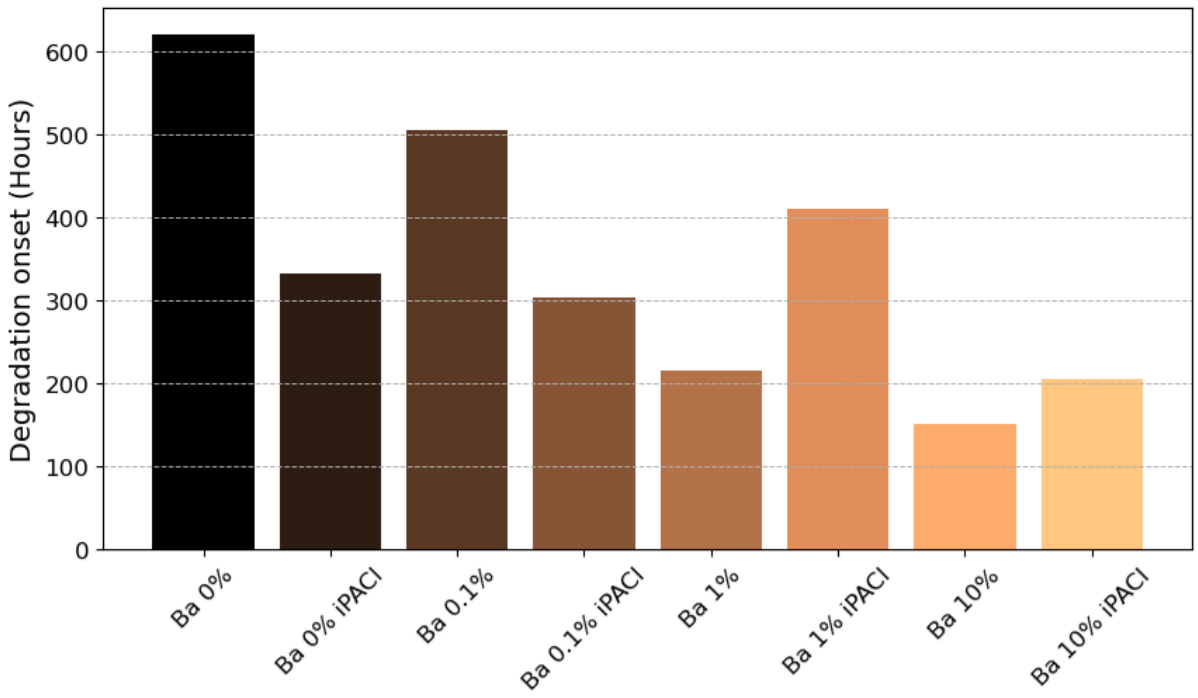

Figure 3.6. Degradation onset time of barium substituted films with and without iPACl

hand with higher Ba substitution ($>$ 1% Ba) it is observed see that the iPACl conditions have higher stability than their without iPACl counterparts. The leading hypothesis here is that the higher amounts of Ba lead to defects in the films that act as centers of degradation. Hence, when looking at the stability of only Ba films, there is a clear downward trend in stability as a function of increasing Ba. iPACl on the other hand promotes crystallization and smoother morphology. However, ultimately the iPACl deprotonates the FA cation, inducing degradation. This is why in the 0 Ba and 0.1% Ba films, the conditions with iPACl fare worse. But at higher concentrations of Ba, the iPACl works to slow down degradation by forming better quality films than the without iPACl films. Hence, it is seen here that the iPACl containing films have better stability in the higher % Ba conditions.

Single Crystal Growth:

As a final attempt to see the possibility of incorporating barium in $FAPbI_3$, single crystals of $FAPbI_3$ are grown using the Solvent Orthogonality Induced Crystallisation (SONIC) method

developed by graduate students in our lab. This would clarify any affect the solution chemistry or processing conditions could have in potentially preventing Ba from substituting Pb in the film. This is a tried and tested method that involves growing pure single crystals of MHPs through slow vapor assisted diffusion of AS into the precursor solution.

Briefly, 1.5M of $FAPb_{0.99}Ba_{0.01}I_3$ and $FAPb_{(1+x)}Ba_{(x)}I_{(3+2x)}$(x = 0.001, 0.01, 0.1) solutions were prepared which were filtered into a 20 ml vial. This 20 ml vial was opened and placed in a 100 ml vial with methyl acetate as an AS. The 100 ml vial was closed and placed in a sand bath at room temperature for about 3 days. The 10% barium condition did not successfully crystallize into $FAPbI_3$ crystals, instead creating layers of BaI_2, FAI and PbI_2. The crystals grown were reclaimed by repeatedly washing and drying with clean unfiltered methyl acetate 6 times. The reclaimed crystals are then dissolved and diluted down to 100 ppm and 100 ppb in 2% aqueous HNO_3 for Inductively Coupled Mass Spectrometry (ICPMS). Here, intensities of Ba is measured in a solution normalized to the intensity of lead using the Kinetic Energy Discrimination (KED) mode that can detect very low concentrations of elements. However, upon performing ICPMS in KED mode on the 4 conditions including control, it was found that the intensity of the Ba was below the instrument detection limit. This indicates little to no Ba in the single crystals despite the latter conditions having an excess of Ba. Hence, unsuccessful Ba incorporation is observed through single crystal growth. Therefore, it is highly possible that the film processing methodology had no impact on incorporation of Ba in the $FAPbI_3$ lattice. There is likely a more fundamentally limiting factor at play, preventing Ba^{2+} substituting Ba^{2+}.

Given the extensive attempts at substituting Ba through thin-film synthesis with excessive Ba and single-crystal growths, it is concluded that the Ba_{2+} cation does not occupy the BX_6 octahedra in $FAPbI_3$. This is likely due to the lack of an np2 lone pair in the outer shell electron of Ba. This is probably why it is unable to coordinate effectively with the I^{2-} anions in the octahedra. This further explains why Sn substitution has been proven successfully upto 50% as Sn has the same np2 lone pair as Pb [43]. Ba was also explored as a possible additive in solution to promote thin film formation. However, it is seen through PL and stability tests that an attempt

at Ba substitution leads to films with poor optoelectronic performance as well as low stability in an oxygen and humidity free environment. It is likely that Ba in the solution acts as an inhibitor for continuous $FAPbI_3$ lattice formation. Moreover, because of this lack of incorporation in the bulk of the film, it induces precipitates on the surface and likely some bulk defects.

3.1.1 Amidinium Chloride Series As High pKa Additives To Stabilize Perovskite Ink and Film

Introduction

PSCs gained a huge boost in performance in 2020 as a result of the pioneering work done by Kim et al. on MACl additives [18]. They demonstrated that MACl can be used as an additive in their perovskite inks to form an intermediate phase that promotes high crystallinity and smooth morphology in their $FAPbI_3$ films.

However, it was later discovered that although MACl boosts initial performance, it proves to be detrimental to the stability of the film. This is because the MA^+ cation reacts with the FA^+ in the solution to create n-methyl formamidinium (nMFA) and hence degrades the optoelectronic quality and phase stability of the MHP thin film [32]. The interaction between MA and FA involves the FA cation being nucleophilically attacked by a deprotonated MA^+ cation, resulting in the formation of nMFA and ammonium. This reaction proceeds through two primary steps: 1) deprotonation of the MA^+ cation to yield methylamine, and 2) nucleophilic attack by methylamine on FA.

However, it was later discovered that although MACl boosts initial performance, it proves detrimental to the stability of the film. This is because the MA^+ reacts with the FA^+ cation in the solution to create n-methyl formamidinium (nMFA), degrading the optoelectronic quality and phase stability of the MHP thin film [32]. The interaction between MA and FA involves the FA^+ cation being nucleophilically attacked by a deprotonated MA cation (methylamine), resulting in the formation of nMFA and ammonium. This reaction proceeds through two primary steps: 1) deprotonation of the MA^+ cation to yield methylamine, and 2) nucleophilic attack by

methylamine on FA.

The acid disassociation constant (pKa) of the additive is inversely proportional to the rate of this reaction, as it dictates the deprotonation of the cation such as MA^+. Hence, an in-house study was carried out on alkylammonium chloride additives with increasing pKa values and chain lengths. Briefly, Ammonium Chloride (NH_4Cl), Methylammonium Chloride (MACl), Ethylammonium Chloride (EACl), Isopropylammonium Chloride, n-Propylammonium Chloride (iPACl), and n-butylammonium chloride (n-BACl) in order of their increasing pKa were used as additives in our baseline $FAbI_3$ ink. Although the study is currently under-review at a peer reviewed journal, it can be revealed that iPACl with pKa of 10.63 [13] displayed a reaction rate with FA^+ ten times slower than MA^+ . Hence, this motivated further exploration of ammonium salts with high pKa values.

The amidinium chloride series are characterized with two amine groups, one of which bonds with a chlorine atom and an R group which could be a carbon chain or another amine. These have been identified in literature as potential candidates for slowing down the deprotonation reaction as a result of their high pKa values. Hence, this study tests the amidinium series, particularly guanidinum (Gua) and acetamidinium (Ac), as solution additives to increase perovskite ink lifetime while also creating perovskite intermediates to support the formation of high crystallinity perovskite films. Gua has a molecular formula of $C(NH_2)_2NH_3Cl$ while Ac has one methyl group replacing the amine group in Gua to form a molecular formula of $C(CH_3)(NH_2)NH_3Cl$ as shown in Fig 3.7.

Upon initially incorporating Gua and Ac as additives in our $FAPbI_3$ ink to fabricate thin films, the formation of potentially disruptive 2D phases is observed. These 2D phases are known to be detrimental to device stability and performance. Subsequently focusing on Gua, an attempt to lower and fine-tune the Gua concentration to prevent any 2D phase formation was made. However, it was found that at sub 1% concentration the PL peak emission slightly shifts and shows no improvement in intensity, indicating defects in the film. At higher concentrations there is again undesirable 2D phase formation. Hence it is determined through these XRD and steady

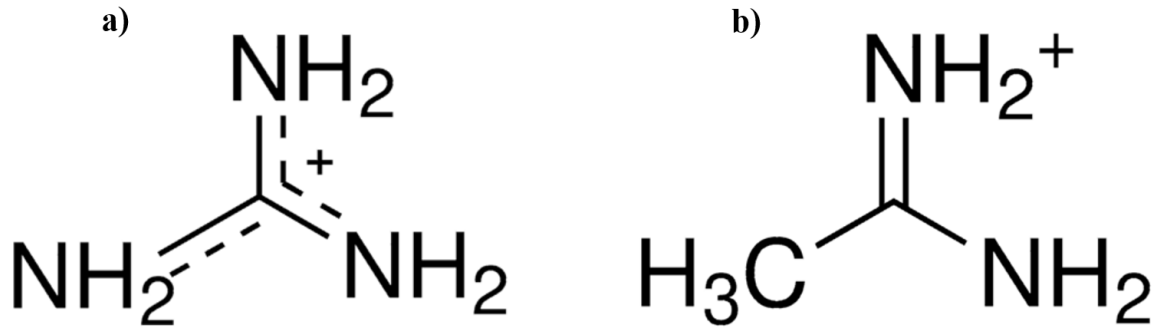

Figure 3.7. Molecular structure of a) guanidinium cation and b) acetamidinium cation

state PL studies that despite the high pKa of Gua and Ac chlorides, the bulky cations cannot successfully form productive intermediate phases instead negatively affecting the optoelectronic qualities of the film.

Initial Investigation

1% or 0.013 M to 5% or 0.06 M of Gua and Ac were incorporated in 1.33 M $FAPbI_3$ in 2ME with 7.5% by volume NMP through PASCAL's solution mixing capabilities. The experiment also included the lab baseline condition of 15% or 0.2 M MACl referred to as 0% Gua. Lower concentrations of Gua and Ac were initially tested due to the much larger size of these amidinium chlorides compared to MACl. It was theorized that higher amidinium concentrations may lead to excessive 2D phase formations in the ink and thin films. The perovskite inks were spin-coated at 8000 RPM for 30 seconds on a glass/MeO-2Pacz stack and then annealed at 150°C for 10 minutes. Steady-state PL on these films were taken after giving ample time to cool down to RT. The results are summarized in Figure 3.8(a). The control has a peak PL intensity of 3×10^4 CPS and a peak position of 1.53 eV. The peak PL intensity of Gua 1% drops down to 1×10^4 and then steadily increases up to 5×10^4 CPS for the 3% Gua condition. The 4% Gua condition is missing in this batch due to operator mishandling. Finally,

the 5% Gua condition drops down to 2×10^4 CPS again. Looking at the peak PL emission energy, the control condition has an average peak PL position of 1.535 eV, which drops down to around 1.520 eV for the 1% Gua condition with a gradual increase to 1.525 eV for the 4% Gua condition stabilising to around the same value for the 5% condition. It is noted with experience, that an increased peak PL intensity accompanied by a small change in PL peak position is generally due a combined effect of defects in the film and an occurrence of a surface passivating phase which could be δ phase $FAPbI_3$, excess PbI_2 or a 2D perovskite [12]. Hence, what could be happening here is the introduction of non-radiative recombination centers by adding a small amount of Gua and the addition of more leads to a passivating phase that steadily increases the peak PL intensity.

Looking at the Ac samples compared to the control; the peak PL intensity drops significantly from the control to 1% Ac. The PL then shows a gentle logarithmic climb to roughly the same value as the control as a function of increasing % Ac . 1% Ac shows a peak PL of 1×10^4 CPS which then increases to 2×10^4 CPS and 3×10^4 CPS for conditions 2 and 3%, respectively. The 4 and 5 %r conditions show an average peak PL intensity of 4.5×10^4 CPS. However, in general, looking at Figure 3.8 (b) the peak PL intensity follows a gentle logarithmically increasing trend. The peak PL emission energy of the Ac films shows a generally linear trend from 1.520 to 1.530 eV after a drop from around 1.535 eV, strongly suggesting the presence of defects in these films creating sub-bandgap energy levels. To elucidate the presence of undesirable phases and to evaluate the crystalline quality of these films, XRD measurements are conducted.

Air-free parallel beam XRD was conducted on these films to further investigate the presence of unwanted phases. The data of the 3% Ac film are missing as it underwent rapid degradation before it could be measured. Looking at the XRD plots in Figure 3.9, the control, Gua, and Ac films show the perovskite cubic phase peaks at $14°2\theta$, $28°2\theta$, and $32°2\theta$ albeit with varying intensities and several non-cubic phase peaks in the Gua and Ac conditions. Non-cubic perovskite $11.5°2\theta$, $12.9°2\theta$, $26°2\theta$, and $29°2\theta$ peaks are observed in the Gua and Ac films, with their intensities increasing as a function of increasing additive percentage. The $12.9°2\theta$

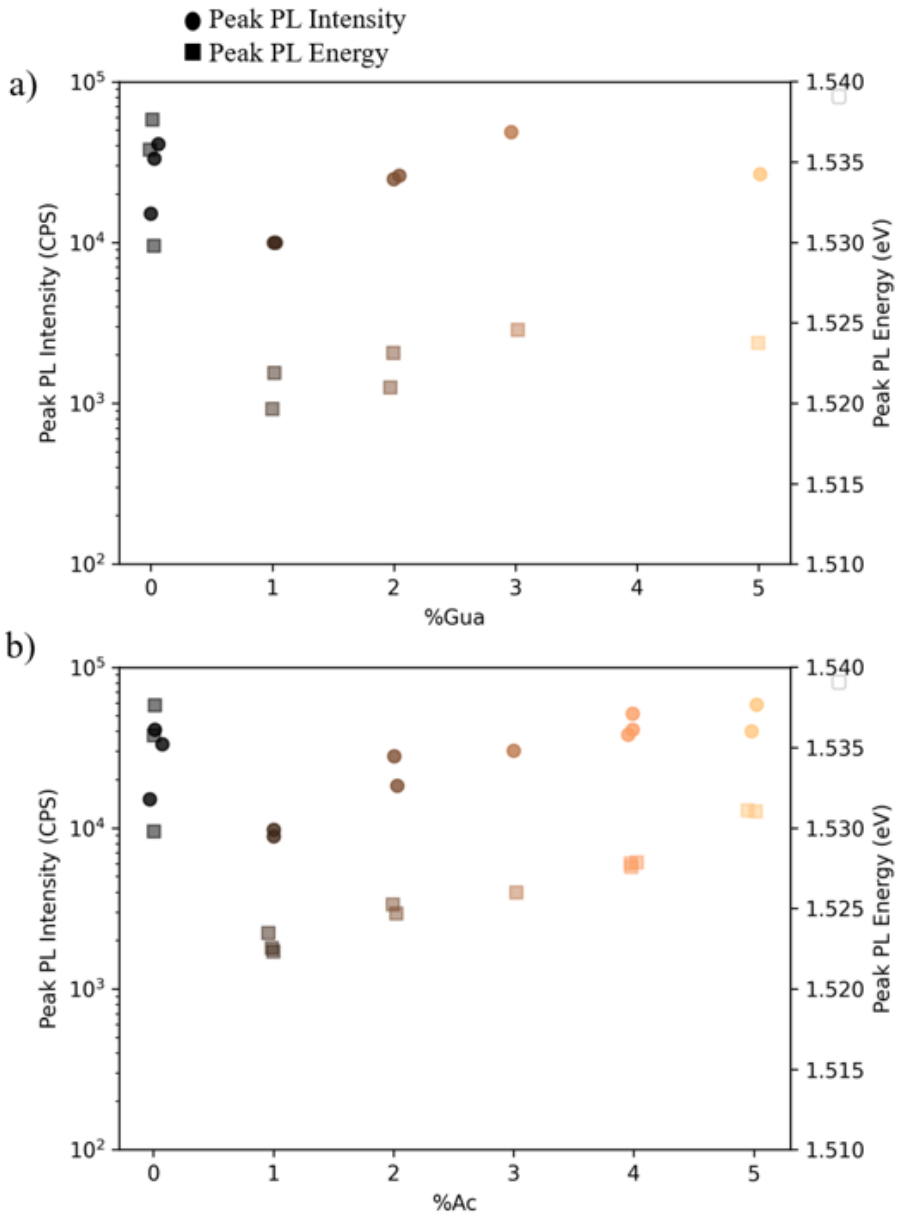

Figure 3.8. Peak PL Intensity and Energy for a) Gua films and b) Ac films

peaks could represent excess PbI_2 that precipitates on the surface of these films. The Ac 5% film shows a sharp peak at 13.3°2θ with an intensity higher than the 14°2θ cubic peak.

It is reasonable practice to refrain from over-analyzing and fitting the remaining peaks as they are likely a result of interaction between multiple components of the ink. However, it is well known in literature that bulky A-site cations lead to 2D phases by preventing the BX_6 octahedra from assembling into a cubic structure, which is likely what is happening here [12]. The possibility is also considered that the 11.5°2θ and 26.2°2θ peaks could be δ phase, which occurs at 12.7°2θ in $FAPbI_3$ but is left-shifted due to Gua or Ac incorporation. The formation of these phases explains the increased PL intensity as a function of increasing amidinium percentage, while the defects formed due to these phases explain the slight peak PL emission shift observed.

Moving forward, attention was brought to sub 1% addition of Gua as the Ac samples showed weak cubic phase peak and high secondary peaks intensities. Hence, 0% to 1% Gua MHP films were fabricated in 0.25% increments with the 0% Gua having 0.2M MACl, making it the control condition. Looking at the PL data in Figure 3.10, it is observed that adding Gua from 0.25 to 0.75% causes a steady drop in PL intensity followed by a big jump to around the same value as the control condition (0.2 M MACl), around 0.8×10^4 CPS for the 1% Gua condition. It is noted that the PL intensity of the control in this batch is lower than the lab baseline which can happen due to unfavorable deposition conditions but it is close in general order of magnitude. Additionally, the control condition has a peak PL emission energy 0.1 eV lower than the previous batch which falls in line with the drop in PL intensity, likely due to the aging of the solutions or the glovebox condition on that day. This phenomenon, batch to batch variation in MHP is well documented in literature [35]. The peak PL emission energy shows a slight increase in energy as a function of increasing Gua from 0.25% to 0.75%. Gua films from 1 to 4% Gua were also fabricated to evaluate the previous results. Similar trends are seen post 1% Gua addition with 4% condition falling in line with the trend from the previous batch, showing a general decrease in PL intensity while exhibiting a slight increase in PL peak position.

To better understand these data, XRD patterns of these films are analyzed, Figure 3.11. It

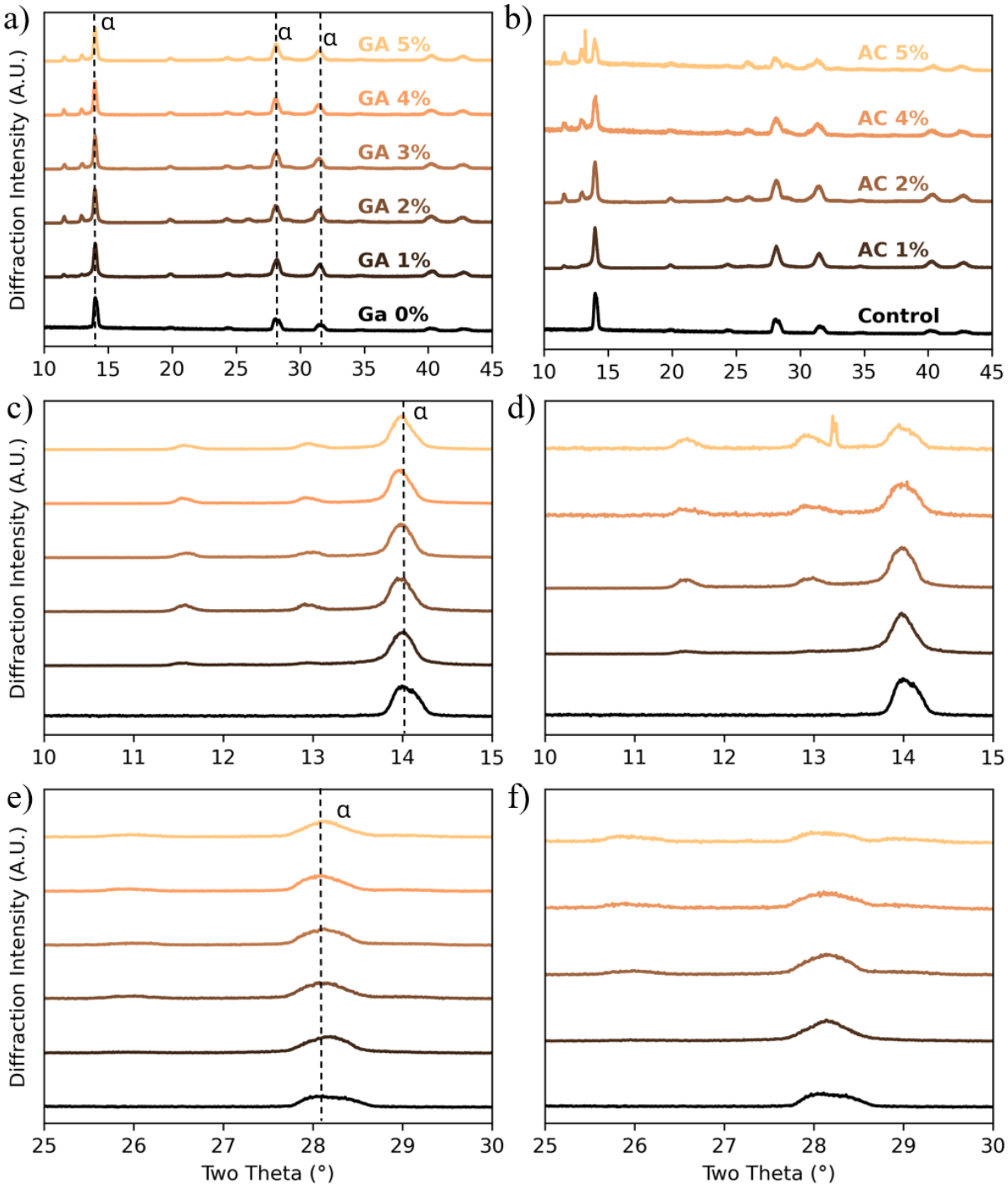

Figure 3.9. XRD patterns for a)c)e) Gua films and b)d)f) Ac films. Here, α refers to the 3C MHP phase peaks where the 14°2θ peak corresponds to the (100) plane.

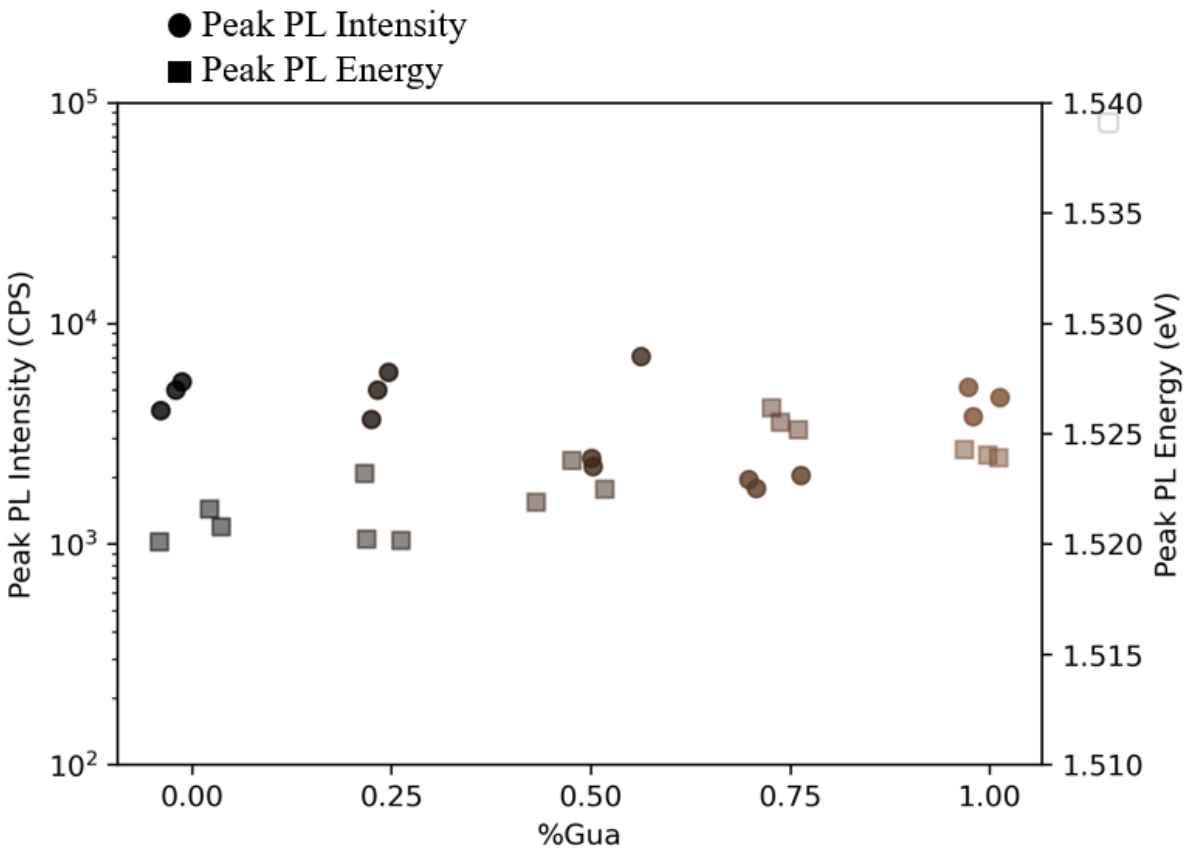

Figure 3.10. Peak PL Intensity and Energy for sub 1% Gua films

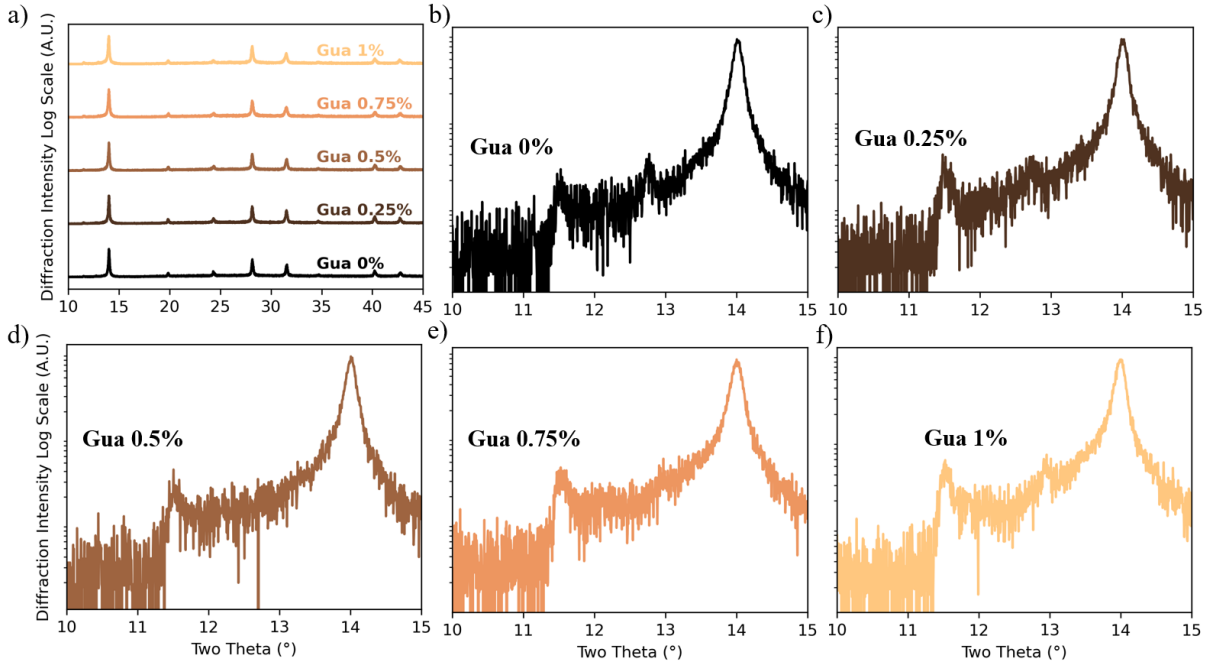

Figure 3.11. a) XRD patterns of Gua films from 10 to 45°2θ b)-f) XRD patterns in log scale of Gua films in order of increasing Gua %

is observed that all of them exhibit standard cubic-$FAPbI_3$ peaks. Furthermore, it is seen that control films show the δ phase and PbI_2 peaks at 11.5 and 12.8°2θ, which could be due to an error in the weighing of the precursors, prolonged exposure when transporting films to air-free XRD, or the processing conditions mentioned earlier. What is more interesting, however, is the increase in intensity and peak position of the 11.5°2θ peaks as a function of % Gua as shown in figure. For Gua % higher than 0.5, the 12.8°2θ peak shifts closer towards 12.9-13°2θ and increases in intensity with the amount of Gua added. Again, over-analyzing these unidentifiable peaks is avoided as the purpose of Gua as an additive is to improve the crystallinity of $FAPbI_3$ thin films. Through two batches of amidinium additives in the perovskite ink, it is observed that these additives undergo various reactions either in the solution state or in the thin film during annealing to produce unwanted phases that have deleterious effects on the crystalline properties and consequently the optoelectronic properties of the film.

3.1.2 Conclusion

Hence, the detrimental effects of adding even a small amount of Gua in the precursor ink is observed as it reduces peak PL intensity or induces passivation effects through what is likely to be 2D phases. The formation of these phases passivate the thin film surface, compensating for the loss in PL due to decreasing crystalline quality. It is concluded that despite the high acid dissociation constant of Gua and Ac, the steric hindrance caused by the large size of the organic cation disrupts the crystallization of $FAPbI_3$. Thus, failing to act as a crystallization boosting additive and instead leaving unwanted phases in the film that could possibly lead to degradation of the photoactive α phase.

3.2 Non-aqueous SnO_x as a Solution Deposited Electron Transport Layer for Inverted Perovskite Solar Cells and a Buffer Layer for Perovskite/Silicon Tandems

3.2.1 Introduction

SnO_2 has been widely used in PSCs as an ETL in standard architecture n-i-p PSCs due to their high electronic conductivity, good optical transparency, wide bandgap, and high chemical stability [40]. However, solvent incompatibility and harsh processing conditions have limited the direct deposition of fully solution-processed SnO_2 in p-i-n devices. For example, SnO_2 is generally deposited on the TCO using techniques such as chemical vapor deposition, atomic layer deposition, or solution-based processes requiring high temperature annealing ($> 150°C$). These deposition methods would severely damage the underlying MHP layer in p-i-n devices. Here, non-aqueous SnO_x nanoparticles (NP) are investigated as a potential replacement for conventional C60/BCP ETL in inverted $FAPbI_3$PSCs. SnO_x also has the potential to act as a buffer layer for sputtered ITO deposition on MHP/Si tandems. SnO_x is used here instead of SnO_2 as the oxidation state of the SnO_x thin film was not analyzed post processing. There is a possibility that a certain percentage of Sn oxidized to its Sn^{2+} state instead of Sn^{4+}.

C60/BCP are most commonly used in p-i-n devices as ETLs but suffer from some drawbacks such as the expensive cost of material, general insolubility in most solvents, and the hydrophobic nature, leading to inhomogeneous and agglomerated films through solution phase depositions [42][24]. To achieve better quality films, C60 can be thermally evaporated in a vacuum chamber which is productivity and financially limiting in the context of terra-watt scale commercialization. In addition, the films that form are still brittle and prone to fracture. This is important because of the need for a buffer layer in the sputtered ITO deposition for MHP/Si tandems. The general architecture for a MHP/Si tandem is an Si bottom cell with PSC deposited on top. A TCO is required on the perovskite for charge extraction in four terminal tandems, and hence, ITO is generally sputtered on the surface of the PSC stack. However, high momentum particles in sputtering damages the C60 ETL and subsequently the MHP. Therefore, an ALD deposited SnO_2 layer is generally deployed to act as a buffer layer. However, ALD is an expensive and time consuming process which is again a barrier for scaling up. Therefore, solution deposited SnO_x with low temperature processing could potentially act as an ETL and a buffer layer for inverted PSC and MHP/Si tandems.

Devices are fabricated by spin coating the non-aqueous acetate functionalized SnO_x nanoparticles as the ETL on the baseline $FAPbI_3$ halfcells. An increased V_{oc} but a lower J_{sc} compared to C60/BCP ETL PSCs (Control) is observed. Through optical and electron microscopy along with a potentiostatic technique, Cyclic Voltammetry (CV), it is determined that pinholes in the SnO_x film lead to significant losses in J_{sc}. To prevent the formation of these pinholes, several processing conditions are implemented; Spin speed and acceleration, anneal time and temperature, varying solution concentration and vacuum assisted film formation. The acetate-functionalized ligands on SnOx nanoparticles cause agglomeration, leading to large holes in the film. This issue does not occur in blade coating, which has gentler deposition conditions compared to the high centrifugal forces seen in spincoating. However, as blade coating is beyond the scope of this study, it was not explored further.

3.2.2 Initial Attempt At Devices

The SnO_x nanoparticles were synthesized by collaborators from the University of Louisville following the methods in their recent publication [6]. Briefly, these are non-aqueous SnO_x nanoparticles synthesized through the widely known sol-gel method which are then ligand-functionalized by acetates and finally dispersed in anhydrous ethanol (EtOH). A 1:20 by volume diluted solution was prepared using the as-received stock solution with anhydrous ethanol as the solvent. PASCAL was used to deposit the baseline half-cell (Glass / ITO / MeO-2Pacz /$FAPbI_3$) on top of which the prepared SnO_x solution was spin-coated. A range of spin coat speeds and anneal times were explored to perform an initial screening of the sensitivity of the fabricated PSCs to SnO_x processing conditions, the details in Table 3.2.2. This experimented is referred to as batch 1. Steady-state PL measurements were taken using PASCAL's characterization line before and after SnO_x deposition to measure and compare the loss in PL with the C_{60}/BCP stack. Figure 3.12 shows peak PL intensity drops to half the original intensity after the deposition of SnO_x, this drop is much smaller than what is observed in the baseline C_{60}/BCP stack where it drops an entire order of magnitude. The perovskite/C_{60} interface sees significant band misalignment due to C60's lower CB energy level which leads to poor radiative recombination in the PL and eventually lower V_{oc} in a PSC. Generally, an order-of-magnitude drop PL leads to a 0.1V drop in V_{oc} in the PSC. Hence, it was expected that the PSC with SnO_x ETL would have a higher V_{oc} than the control.

Upon finishing the PSC with metallic contacts, their JV curves were taken, Figure 3.13 b) and c) show the architecture of the SnO_x and C60/BCP baseline devices respectively. Figure 3.13 a) shows the JV curves of SnO_x with all the different deposition conditions. Compared to the baseline C_{60}/BCP, the SnO_x devices show a 0.1 V higher V_{oc} as expected but show lower J_{sc} by 3-4 mA/cm^2 and 55% FF compared to 75%. The SnO_x devices show significant hysteresis, especially in lower applied voltage conditions. The reverse scans observe severe shunting compared to the forward scans. There is some variability amongst the various conditions

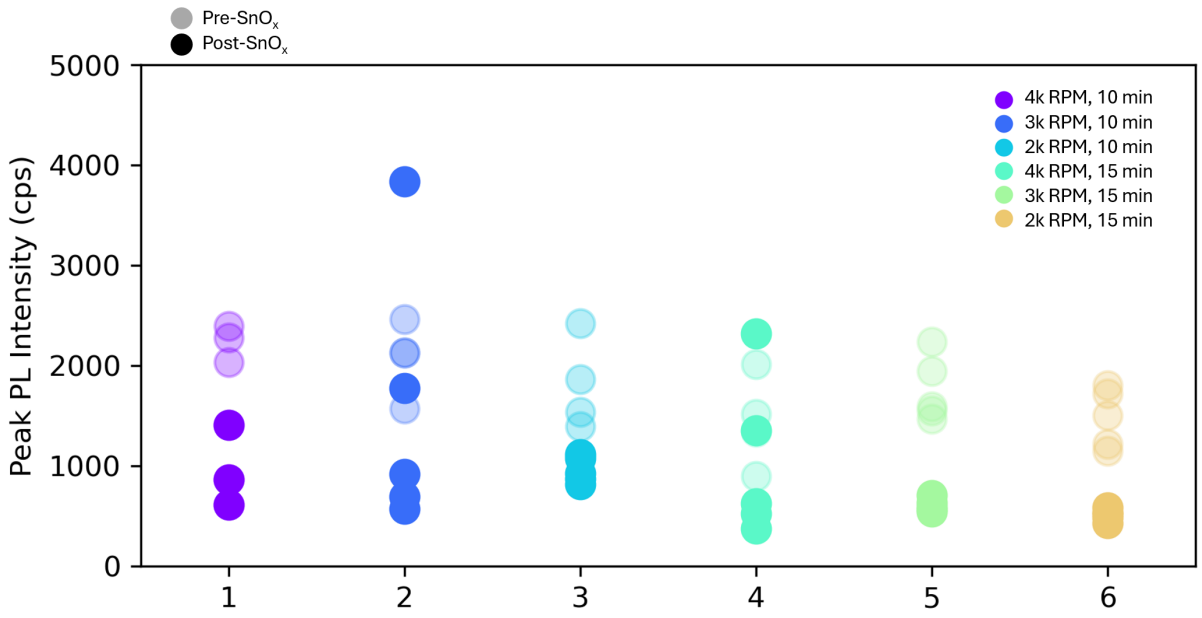

Figure 3.12. Peak PL Intensity of Glass/MeO-2Pacz/$FAPbI_3$ befoer and after SnO_x deposition

Table 3.1. Batchwise Summary of Processing Conditions Used to Improve Morphology of SnOx Films.

Batch	SnOx Diln. in EtOH	Spin Speed (RPM$\times 10^3$)	Spin Acc. (RPM/s)	Anneal Temp. (C)	Anneal Time (Min)	Vac. Cryst.
1	1:20	2, 3, 4	500	100	10, 15	No
2	1:10, 1:20	2, 4	125, 250, 500	100	10, 15	No
3	1:20	2	500	80, 100, 140	10	No
4	1:20	2	500	80, 100, 140	10, 30	Yes
5	1:20, 1:25, 1:30, 1:35	2, 4	500	100	10	No

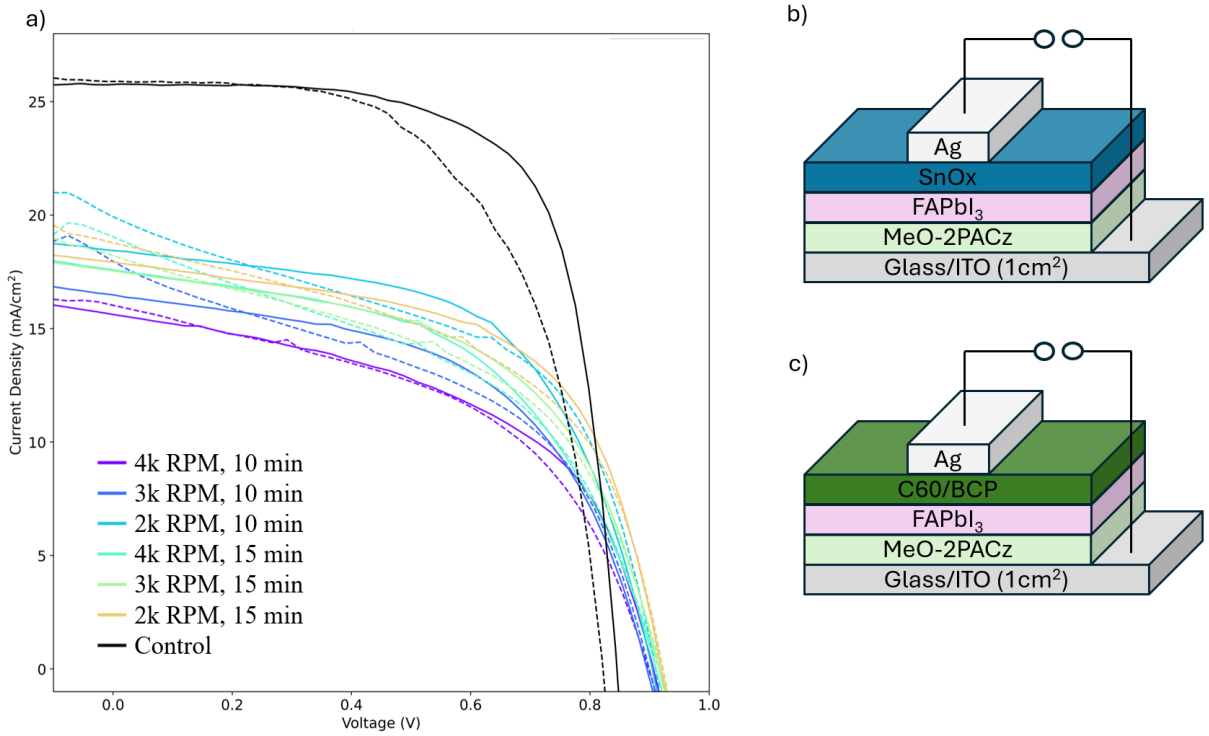

Figure 3.13. a) JV Curves of the SnO_x Batch 1 PSC, Architecture of b) SnO_x PSC c) baseline C60/BCP PSCs

explored. However, the J_{sc} is dangerously low across the board so overanalyzing the data is avoided before the main issue is solved. This warranted further investigation on the potential causes for this loss in performance using CV and microstructural analysis of SnO_x films.

3.2.3 Investigating The Electronic And Morphological Properties of SnO_x Film

CV has been shown to be a reliable and time efficient method to screen the electronic and morphological properties of charge transport layers in PSCs. Cyclic voltammetry is a common method used in electrochemistry to determine the oxidation and reduction potentials of electrolyte solutions. It involves performing a sweep of applied potentials in a range of positive and negative values while measuring the current flowing through the electrodes, the onset of current depending on the polarity of the applied potential indicates the oxidation or reduction potential of the electrolyte. In the setup used in these experiments, solution deposited SnO_x on

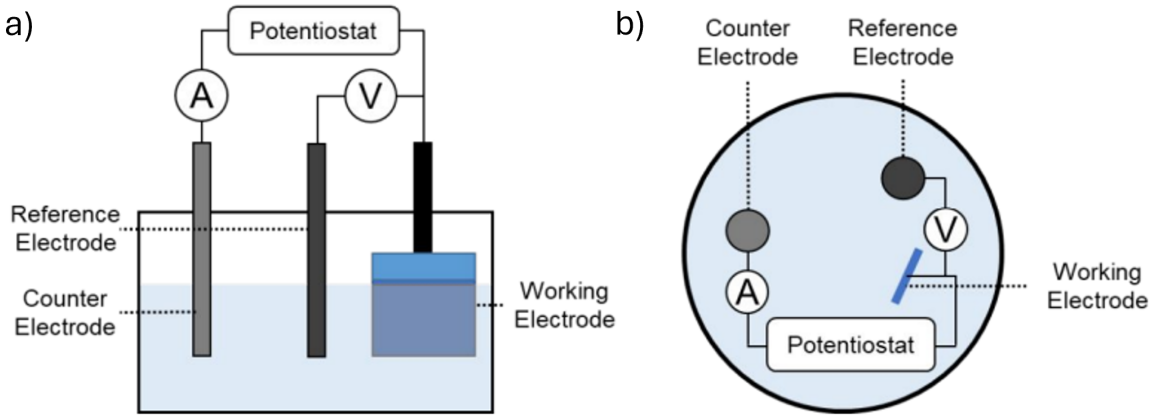

Figure 3.14. Cross-sectional view of the 3-electrode CV setup b) Top view of the same setup [19]

ITO is used as one of the electrodes in a 1.0 mM ferri-/ferrocyanide outer-sphere redox couple along with a 0.5 M KCl supporting electrolyte, which gives us a semiconductor-electrolyte junction. Here, a single junction silver chloride (AgCl) reference electrode immersed in saturated potassium chloride is used with a standard platinum (Pt) counter electrode as a reference and counter electrode respectively. The three electrode setup is shown in Figure 3.7, where the working electrode, or the ITO/SnOx film faces the counter electrode and the potentiostat applies a voltage between the working and reference electrode and the current is measured from the counter electrode.

In the case of bare ITO, it is a standard CV setup and on sweeping potentials a classic CV duck curve is obtained which will be referred to as the ITO duck curve in this chapter, See Figure 3.15. It essentially reflects the redox potential of the electrolyte where there is a sharp anodic and cathodic current onset peak near 0 V followed by a relatively flat curve in the high magnitude potential regions. In the case of a conformally coated SnO_x semiconductor layer demonstrated by Kodur et al, the cathodic onset of current is pushed to more negative regions (higher magnitude) because of the difference in energy level of the CB and VB of the SnO_x. In particular, the band bending effect of SnO_x at the surface leads to a sharp onset of the cathodic current (negative potential). This onset potential relates to the V_{oc} of the fabricated PSC as it

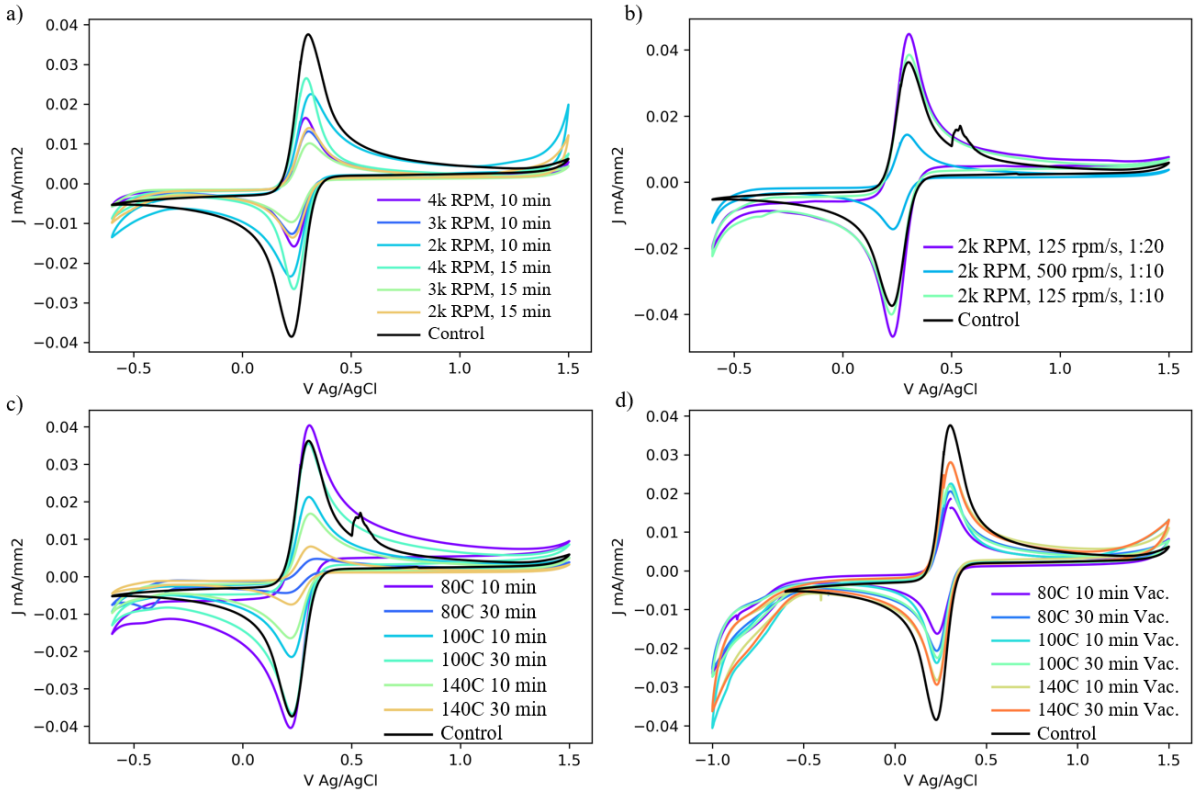

Figure 3.15. CV curves of Glass/ITO/SnO_x a) batch 1 b) batch 2 c) batch 3 d) batch 4

corresponds to the band alignment of the absorber and ETL, where the closer the CBM, the lower the loss in energy of the electrons and hence a higher V_{oc}. Furthermore, the shape of the curve during the anodic sweep or positive applied potential can give essential information on the J_{sc} of the PSC. A perfect film with no pinholes or other deformities that could lead to current leakage shows no anodic current, whereas defective films show the onset of anodic current.

Upon performing CV on ITO/SnOx films, it is observed that the CV curves look just like the shape of bare ITO duck curves, Figure 3.15 a). This was hypothesized to be due to microscopic pinholes in the film that could lead to the electrolyte making direct contact with the ITO under the SnO_x, essentially registering an ITO duck curve. Hence, SEM images were taken of the SnO_x films, Figure 3.16. The SEM clearly show around 10nm diameter pinholes scattered throughout the surface of the SnOx films in all processing conditions. These pinholes explain the loss in J_{sc} in the SnO_x devices. Hence, in an effort to prevent pinhole formation, several

processing conditions were experimented.

Tuning Processing Conditions to Improve SnO_x Film Morphology

Batch 2

Table 3.2.2 summarizes the processing conditions attempted in batch 2 to improve the morphology of the SnO_x films. Here, the dilution amount was halved to create a thicker more viscous film with the hypothesis that the film wouldn't stretch out too thin and the SnO_xwould agglomerate in a more compact fashion. Additionally, the acceleration was slowed down as well to reduce centrifugal forces on the film, aimed at increasing the thickness of the film and keeping the SnO_x more tightly bound. Anneal time and temperature were kept the same as the previous batch. All the SnO_x films were spun on ITO for CV measurements. Here, CV is used as a screening method to gauge the effectiveness of our processing conditions in reducing pinholes. This is a more efficient route to characterising the SnO_x films particularly in our attempts to reduce pinhole formation. Through CV measurements, Figure 3.15 b) it was determined that the film still had several leakage points, still registering ITO duck curves during the CV measurements.

Batch 3

For batch 3, an attempt was made to change the solvent evaporation process by tuning the annealing process while keeping the spin conditions the same as Batch 1. Three temperatures were tested, 80°C, 100°C, and 140°C, to measure the effect of evaporation rate on the film morphology. It was hypothesized that a slower evaporation rate from a low temperature could lead to gentler film formation and hence a compact film. Conversely, a higher temperature should lead to fast boiling off of the EtOH and hence several morphological defects. Looking at the CV curves in Figure 3.15 c), it is evident that this is the ITO duck curve again. Although there are some changes in the shape of the curve for different annealing conditions, for the purposes of an ETL, the films have too many leakage points.

Batch 4

After this, in batch 4, a top to bottom crystallisation was attempted by placing the films in a vacuum chamber for 5 minutes after the spin coating step. The films were then annealed with the same steps as in batch 3. The hypothesis here was that the EtOH would evaporate out of the spin coated film from the top rather than the bottom in annealing due to the vapor pressure difference possibly leading to a more compact film. Here again, it is observed in Figure 3.15 d) that the CV curves still show the ITO duck curve shape. The CV curves do exhibit different behaviours towards higher absolute potential difference regions, this is could be due to the electrolyte preparation and age which can have an effect on the measurement. It could also be a consequence of the top to bottom evaporation. However, our main concern here is the two duck curve peaks near 0 V which need to be pushed towards higher potential regions to exhibit a well functioning ETL.

Batch 5

Finally, in batch 5, a lower concentration spread was attempted with the hypothesis of lower concentrations would spread more easily and form a uniform film through favorable ligand-ligand interactions as it is known that ligand-ligand solution interactions are sensitive to their concentrations [15]. Here, dilutions of 1:20, 1:25, 1:30 and 1:35 are attempted. As a sanity check of whether the CV measurements were actually indicative of ETL performance, PSCs with these conditions were fabricated and SEM images of these SnO_x films were taken. The SEM in Figure 3.16 reveals large cracks and pinholes on the surface of the films.

Consequently, the JV curves of these devices show significant loss in J_{sc} and FF from the baseline. More hysteresis is observed than the PSCs from batch 1, Figure 3.17. These results indicate that the lower dilutions likely lead to thinner films with the SnO_x particles being pulled apart by the centrifugal forces during spin coating. The SnO_x NPs were determined to be incompatible with spin coating due to them possibly having very weak ligand-ligand interactions that could not stand the mechanical stress induced by spin coating. These NPs do not face the same fate during blade coating as it is a very gentle spreading technique that allows the SnO_x nanoparticles to stay uniformly connected throughout the film.

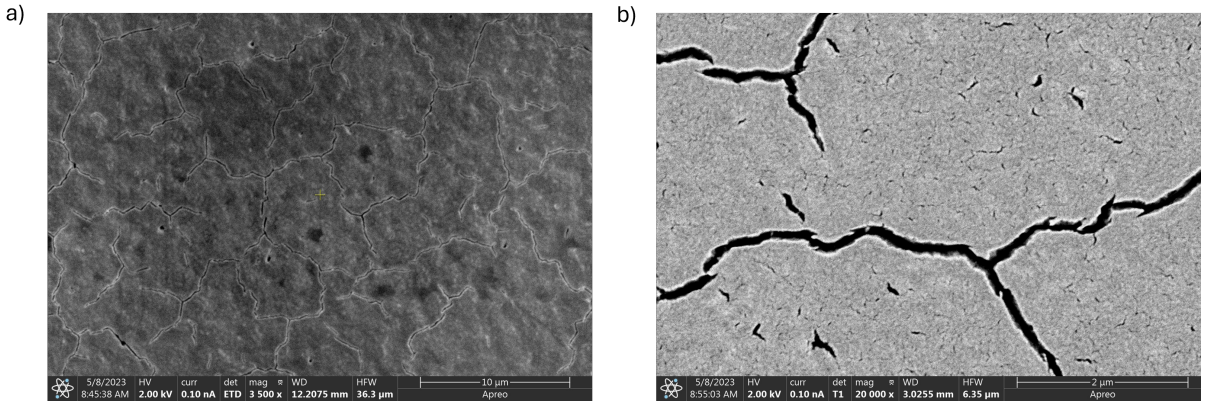

Figure 3.16. SEM image of 1:20 Diln, 2K RPM SnO_x on ITO at a) 3.5kx magnification and b) 20kx amgnification revealing cracks and pinholes on the surface of the films

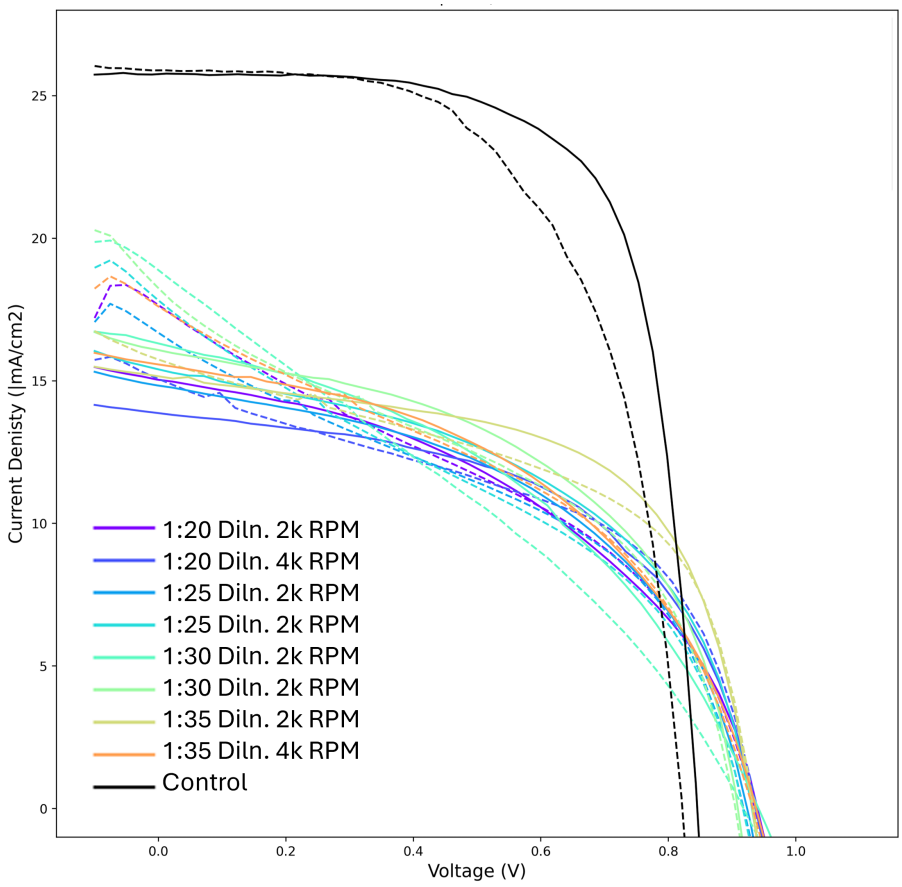

Figure 3.17. JV Curves of PSCs fabricated in B5

3.2.4 Conclusion

In conclusion, an attempt to integrate non-aqueous SnO_x as an ETL in p-i-n PSC architecture is made to improve performance and scalability. An increased V_{oc} through ideal energy level alignment with our absorber is observed. However, significantly lower Jsc in the SnO_x PSCs is observed due to a high density of pinholes. CV is introduced as an efficient method to rapidly screen SnO_x ETLs by detecting pinhholes through a cathodic peak onset. Across 5 batches of varying processing parameters, it is determined that ligand functionalized SnO_x NPs are incredibly prone to separation likely due to their unfavorable NP-NP interaction in solution. Hence, it is likely that these NPs are not possible to integrate with the p-i-n fabrication process.

Chapter 4

Contributions Towards High Volume Degradation Testing

4.1 Custom Hotplate for Light and Heat for Degradation Testing (ISOS-L2) of Perovskite Films

An ISOS-L2 setup was built in-house to integrate durability testing of the perovskite films and devices fabricated by PASCAL. The setup was built based on the standards described for L2 testing in the ”Consensus statement for stability assessment and reporting for perovskite photovoltaics based on ISOS procedures [17]. Briefly, the MHP or PSC must be heated to 65 or 85°C under 1 Sun light intensity in an inert environment. The setup is shown with the key components highlighted in Figure 4.1. It consists of a light housing made from aluminum T-slot extrusions and two white light LED panels calibrated to 1000 W/m^2. A die-cast environmental enclosure is used to house the samples and hot plate. A 6” x 6” window is laser cut on the enclosure lid, and a glass window is carefully epoxied to allow light in. A constant N_2 gas purge is maintained with appropriate gas fittings while ensuring any part that is going in and out of the box is tightly sealed with epoxy.

I was tasked with designing a hotplate for this setup to ensure maximum use of space in the enclosure as well as carefully control of the temperature. The design and layout of the hotplate can be seen in Figure 4.1 (a). A 1/8” aluminum sheet is laser cut in the shape of a 6” x 7” rectangle with holes for screws to hold the stack together. Aluminum is used here due to

its impressive thermal conductivity ensuring efficient heat transfer between the bottom and top surface. The thickness of the aluminum sheet was optimized using basic heat transfer analysis to strike a balance between thermal momentum to stabilise surface temperatures but also ensure a reasonable response to temperature changes from the bottom surface.

A silicone rubber heating pad is attached to the bottom of the top aluminum sheet using a generous amount of homogeneously spread thermal glue. The thermal glue ensures efficient heat transfer between the silicone and aluminum surface. A Pt100 RTD (Resistance Temperature Detector) is used to track the temperature of the hotplate. It is placed between the heating pad and aluminum sheet with the active area facing the aluminum sheet to accurately track its temperature. An RTD is used here over a thermocouple due to the nature of the electronic connections in this setup. Since the PID controller (Process Integral Derivative) cannot be placed in the enclosure, the electrical connections need to be routed out through a DB37 cable, which has 37 exposed leads on one end and a D-Sub connector with 37 pins on the other end. Making a junction in a thermocouple circuit with dissimilar metals can lead to signal noise and hence an inaccurate reading, hence an RTD is used here.

A fiberglass sheet is stacked below the silicone heating pad to prevent heat losses from its bottom surface in an effort to efficiently transfer heat to the top aluminum plate, the active area of the hotplate. The stack is completed with an aluminum sheet of the same thickness sandwiching all the layers from the bottom. Finally, 4 M5 screws are fed from the top aluminum sheet down to the bottom one and screwed into appropriately sized nuts. This design maximizes silicone heating pad - top aluminum sheet contact area through a constant mechanical force. This holds the hotplate together like a sandwich with the intent to maintain long term usage of these hot plates. If only thermal glue was relied on for adhesion, the silicone pad would eventually start losing strong thermal contact with the aluminum sheet, leading to in-homogeneous and inaccurate surface temperature of the hotplate.

The DB37 cable is fed into the enclosure through a drilled hole with both ends carefully epoxied to prevent any air flow in and out. The DB37 is then routed into a breakout board.

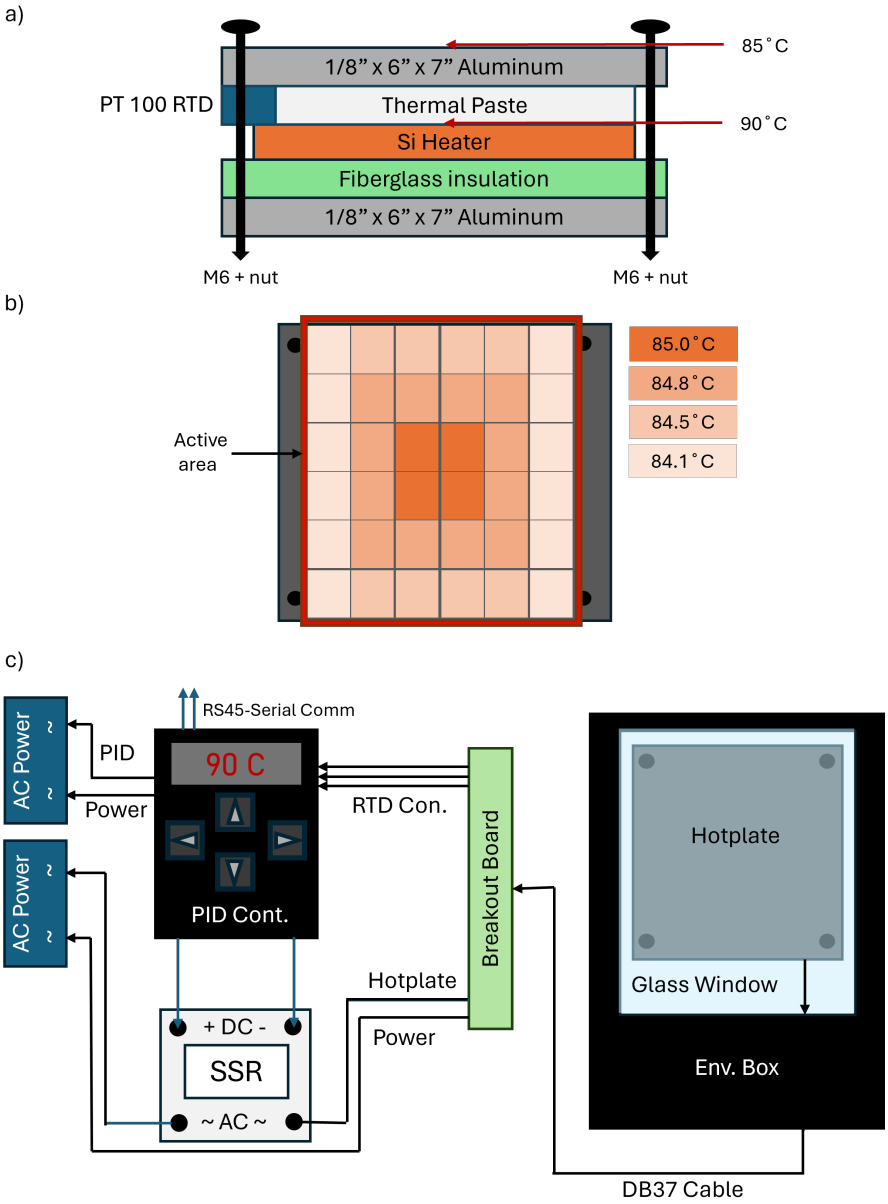

Figure 4.1. a) Cross-section of the hotplate b) Surface uniformity of hotplate active area c) Representative schematic of the wiring in the ISOS-L2 setup

Connections are made from the breakout board to a 120V AC wall socket, PID and an SSR (Solid State Relay). The circuit diagram is explained in figure blah. To explain briefly, the SSR acts as a switch on one of the power terminals of the heater. The 3 wire connections from the RTD are fed into the PID allowing it to read the temperature of the bottom surface of the top aluminum sheet. As the PID controller tracks temperature, it can send signals to the SSR to turn on and off based on PID control principles which stabilizes to the set point temperature. The PID used here comes with an auto-tune function which automatically tunes PID values based on the heater power and RTD response.

There is an offset between the surface of the top aluminum sheet and its bottom. This offset stands at 5°C for a temperature of 85°C, and hence this is accounted for when setting the temperature for an experiment. Furthermore, the surface temperature of the hotplate was mapped under 1 Sun light at 85°C to measure homogeneity, and only a 1 °C difference was found across its 6" x 6" active area, see Figure 4.1 b).

Further, the PID can be individually controlled using MODBUS protocols over RS485 serial communication interface through a custom Python script. This script converts standard decimal to a hexadecimal message which it sends out to the PIDs connected to the RS485 connection. The elegant part of this setup is the fact that all the PIDs feed through only one serial connection which means only one RS485 to USB cable is needed for upto 32 PIDs. The hexadecimal message the Python script sends out holds the address of the particular PID as well as the command such as read temperature, set temperature, etc. The user can set these parameters through the script and send out commands to specific PIDs. This script can be found in the Fenning Research Group Github.

The custom and modular nature of this hotplate served to be incredibly useful when a larger hotplate of active area 12" x 12" was required to be built for another ISOS-L2 setup for degradation testing MHP mini-modules. Here the basic electronic concepts remained the same apart from a change from RTD to thermocouples. Thermocouples could be used in this scenario because the mini-modules come encapsulated hence there was no need for an environmental

enclosure. Additionally, I was able to build out these hotplates with a larger surface area through aluminum sheets of same thickness and a 12" x 12" silicone heating pad. The offset was again measured to be around 5 C and the surface in-homogeneity was found to be +/- 3°C due to the larger inactive area of the hotplate acting as a heat sink to the atmosphere.

4.1.1 Automated Degradation Tracking of Perovskite Films

In the first iteration of the ISOS-L2 setup, expensive GoPro's around costing around $250 each were used to track degradation of MHP film. A picture would be taken every 20-30 minutes as the filsm degrade from α-$FAPbI_3$ to δ-$FAPbI_3$, their color changing from black to yellow. The colormetrics algorithm described in chapter 2 was then performed on the series of images taken over the course of the experiment. However, data had to be manually transferred from an SD card in the GoPro to a computer. The major problem faced here was that the progress of the experiment could not be tracked in real time. To perform colormetric analysis on the films, the ongoing experiment would have to stopped so the SD card can be removed.

Hence, I designed a setup that uses USB cameras controlled by a custom Python script to take pictures at desired intervals. The goal was to individually control up to 4 cameras in running independent experiments, with controlled exposure level, saving the pictures to the desired folder on the laboratory cloud sotrage. This would also feed into our larger meta-database that tracks and trains machine learning models on all the quantitative data obtained from experiments across the lab.

To achieve this a Python package called OpenCV was used that provides a vast range of image and video processing tools while also providing lower level control of compatible USB cameras. For this setup a $50 USB camera was identified that is compatible with OpenCV from ArduCam on Amazon. A control script was developed on Python that identifies and communicates with 4 of these cameras. The most challenging hurdles in developing this script was independently controlling multiple cameras through only one USB port. USB ports lead internally to a USB bus which are notorious for having very low data bandwidth that is a major

limiting factor for our purpose. Holding connections with a camera through OpenCV requires significant data bandwidth. Hence, connecting to more than one camera would overload the USB bus and cause the program to crash. Although there maybe several USB-A and USB-C ports in a computer, there generally is only one or two USB buses. Additionally, the other USB ports are needed to control the PID for the hotplates and in the future the control system for MPP tracking.

Hence, an algorithm was developed to connect to a camera only when a picture needs to be taken, maintaining connections for only about 4-5 seconds per picture. Over the course of 20-30 minutes, multiple cameras can be connected and disconnected through one USB port without exceeding its bandwidth. Hence, the Python script contains a class with the required functions to initiate and stop experiments, where multiple instances of the same class are internally initialized and controlled independently. This is a technique known as multithreading and is a powerful tool for running multiple tasks in python.

The script includes several features to ensure each picture remains in focus and free of blank frames. When using OpenCV to manage cameras, establishing or re-establishing a connection resets all previous settings, including auto-focusing and exposure values. Consequently, each time a picture is taken, the script captures five successive images, using the final one to enable the camera to auto-focus appropriately.

Furthermore, it was observed that upon establishing a new connection, the initial images captured were entirely blank. To tackle this issue, OpenCV's built-in image processing tools were leveraged. The images are converted to grayscale and the percentage of completely black pixels is measured. Only pictures with less than 10% black pixels are retained for further processing.

Presently, the script runs through a Python terminal. However, there are plans to integrate it with an indoor version of PARASOL and develop a custom graphical user interface (GUI) to enhance usability. The script is open-source and accessible on the Fenning Research Group GitHub repository.

Bibliography

[1] 9 - silicon. In N.N. GREENWOOD and A. EARNSHAW, editors, *Chemistry of the Elements (Second Edition)*, pages 328–366. Butterworth-Heinemann, Oxford, second edition edition, 1997.

[2] Nikolai A Belich, Andrey A Petrov, Pavel A Ivlev, Natalia N Udalova, Alla A Pustovalova, Eugene A Goodilin, and Alexey B Tarasov. How to stabilize standard perovskite solar cells to withstand operating conditions under an ambient environment for more than 1000 hours using simple and universal encapsulation. *Journal of Energy Chemistry*, 78:246–252, 2023.

[3] Deniz N Cakan, Rishi E Kumar, Eric Oberholtz, Moses Kodur, Jack Palmer, Apoorva Gupta, Ken Kaushal, Hendrik M Vossler, and David P Fenning. Pascal: the perovskite automated spin coat assembly line accelerates composition screening in triple-halide perovskite alloys. *Digital Discovery*, 2024.

[4] Pietro Caprioglio, Fengshuo Zu, Christian M Wolff, José A Márquez Prieto, Martin Stolterfoht, Pascal Becker, Norbert Koch, Thomas Unold, Bernd Rech, and Albrecht. High open circuit voltages in pin-type perovskite solar cells through strontium addition. *Sustainable Energy & Fuels*, 3(2):550–563, 2019.

[5] Shun-Hsiang Chan, Ming-Chung Wu, Kun-Mu Lee, Wei-Cheng Chen, Tzu-Hao Lin, and Wei-Fang Su. Enhancing perovskite solar cell performance and stability by doping barium in methylammonium lead halide. *Journal of Materials Chemistry A*, 5(34):18044–18052, 2017.

[6] Sashil Chapagain, Pakanati S Chandrasekhar, Deborah McGott, Rosemary C Bramante, Maikel FAM van Hest, Matthew O Reese, Thad Druffel, and Craig A Grapperhaus. Direct deposition of nonaqueous sno2 dispersion by blade coating on perovskites for the scalable fabrication of p–i–n perovskite solar cells. *ACS Applied Energy Materials*, 4(10):10477–10483, 2021.

[7] Hao Chen, Cheng Liu, Jian Xu, Aidan Maxwell, Wei Zhou, Yi Yang, Qilin Zhou, Abdulaziz S. R. Bati, Haoyue Wan, Zaiwei Wang, Lewei Zeng, Junke Wang, Peter Serles, Yuan Liu, Sam Teale, Yanjiang Liu, Makhsud I. Saidaminov, Muzhi Li, Nicholas Rolston, Sjoerd Hoogland, Tobin Filleter, Mercouri G. Kanatzidis, Bin Chen, Zhijun Ning, and Edward H. Sargent. Improved charge extraction in inverted perovskite solar cells with dual-site-binding ligands. *Science*, 384(6692):189–193, 2024.

[8] He Dong, Chenxin Ran, Weiyin Gao, Mingjie Li, Yingdong Xia, and Wei Huang. Metal halide perovskite for next-generation optoelectronics: progresses and prospects. *ELight*, 3(1):3, 2023.

[9] Sean P Dunfield, Lyle Bliss, Fei Zhang, Joseph M Luther, Kai Zhu, Maikel FAM van Hest, Matthew O Reese, and Joseph J Berry. From defects to degradation: a mechanistic understanding of degradation in perovskite solar cell devices and modules. *Advanced Energy Materials*, 10(26):1904054, 2020.

[10] FAO. The impact of disasters on agriculture and food security 2023: Avoiding and reducing losses through investment in resilience, 2023.

[11] Lyubov A Frolova, Denis V Anokhin, Kirill L Gerasimov, Nadezhda N Dremova, and Pavel A Troshin. Exploring the effects of the pb2+ substitution in mapbi3 on the photovoltaic performance of the hybrid perovskite solar cells. *The journal of physical chemistry letters*, 7(21):4353–4357, 2016.

[12] Zeynep Gozukara Karabag, Aliekber Karabag, Ummugulsum Gunes, Xiao-Xin Gao, Olga A Syzgantseva, Maria A Syzgantseva, Figen Varlioglu Yaylali, Naoyuki Shibayama, Hiroyuki Kanda, and Alwani Imanah Rafieh. Tuning 2d perovskite passivation: Impact of electronic and steric effects on the performance of 3d/2d perovskite solar cells. *Advanced Energy Materials*, 13(45):2302038, 2023.

[13] HK Hall Jr. Correlation of the base strengths of amines1. *Journal of the American Chemical Society*, 79(20):5441–5444, 1957.

[14] IEA. World energy outlook 2023. https://www.iea.org/reports/world-energy-outlook-2023, 2023. Licence: CC BY 4.0 (report); CC BY NC SA 4.0 (Annex A).

[15] Jacob N. Israelachvili. *Intermolecular and Surface Forces*. Academic Press, Oxford, 3rd edition, 2011.

[16] Rodolfo Keesey, Armi Tiihonen, Alexander E Siemenn, Thomas W Colburn, Shijing Sun, Noor Titan Putri Hartono, James Serdy, Margaret Zeile, Keqing He, and Cole A Gurtner. An open-source environmental chamber for materials-stability testing using an optical proxy. *Digital Discovery*, 2(2):422–440, 2023.

[17] Mark V Khenkin, Eugene A Katz, Antonio Abate, Giorgio Bardizza, Joseph J Berry, Christoph Brabec, Francesca Brunetti, Vladimir Bulović, Quinn Burlingame, and Aldo Di Carlo. Consensus statement for stability assessment and reporting for perovskite photovoltaics based on isos procedures. *Nature Energy*, 5(1):35–49, 2020.

[18] Minjin Kim, Gi-Hwan Kim, Tae Kyung Lee, In Woo Choi, Hye Won Choi, Yimhyun Jo, Yung Jin Yoon, Jae Won Kim, Jiyun Lee, and Daihong Huh. Methylammonium chloride induces intermediate phase stabilization for efficient perovskite solar cells. *Joule*, 3(9):2179–2192, 2019.

[19] Moses Kodur, Rishi E. Kumar, Yanqi Luo, Deniz N. Cakan, Xueying Li, Michael Stuckelberger, and David P. Fenning. X-ray microscopy of halide perovskites: Techniques, applications, and prospects. *Advanced Energy Materials*, 10:1903170, 7 2020.

[20] Akihiro Kojima, Kenjiro Teshima, Yasuo Shirai, and Tsutomu Miyasaka. Organometal halide perovskites as visible-light sensitizers for photovoltaic cells. *Journal of the American Chemical Society*, 131(17):6050–6051, 2009. PMID: 19366264.

[21] Ravinder Kour, Sandeep Arya, Sonali Verma, Jyoti Gupta, Pankaj Bandhoria, Vishal Bharti, Ram Datt, and Vinay Gupta. Potential substitutes for replacement of lead in perovskite solar cells: a review. *Global Challenges*, 3(11):1900050, 2019.

[22] H. Lee and J. Romero. Climate change 2023: Synthesis report. contribution of working groups i, ii and iii to the sixth assessment report of the intergovernmental panel on climate change, 2023.

[23] Zhen Li, Mengjin Yang, Ji-Sang Park, Su-Huai Wei, Joseph J Berry, and Kai Zhu. Stabilizing perovskite structures by tuning tolerance factor: formation of formamidinium and cesium lead iodide solid-state alloys. *Chemistry of Materials*, 28(1):284–292, 2016.

[24] Hao-Sheng Lin, Il Jeon, Rong Xiang, Seungju Seo, Jin-Wook Lee, Chao Li, Amrita Pal, Sergei Manzhos, Mark S Goorsky, and Yang Yang. Achieving high efficiency in solution-processed perovskite solar cells using c60/c70 mixed fullerenes. *ACS applied materials & interfaces*, 10(46):39590–39598, 2018.

[25] Chong Liu, Wenzhe Li, Jiandong Fan, and Yaohua Mai. A brief review on the lead element substitution in perovskite solar cells. *Journal of energy chemistry*, 27(4):1054–1066, 2018.

[26] Mordor Intelligence. Solar Cell Market Size, Share & Trends Analysis Report, 2022. Report ID: 978-1-68038-691-2, Number of Pages: 82, Format: Electronic (PDF), Historical Data: 2013-2015.

[27] NASA. The POWER Project, 2024. Accessed: 2024.

[28] Jaewang Park, Jongbeom Kim, Hyun-Sung Yun, Min Jae Paik, Eunseo Noh, Hyun Jung Mun, Min Gyu Kim, Tae Joo Shin, and Sang Il Seok. Controlled growth of perovskite layers with volatile alkylammonium chlorides. *Nature*, 616(7958):724–730, 2023.

[29] PV Education. IV Curve, 2024. Accessed: 14 May 2024.

[30] M.M. Rahman, S. Salehin, S.S.U. Ahmed, and A.K.M. Sadrul Islam. Chapter two - environmental impact assessment of different renewable energy resources: A recent development. In Mohammad G. Rasul, Abul kalam Azad, and Subhash C. Sharma, editors, *Clean Energy for Sustainable Development*, pages 29–71. Academic Press, 2017.

[31] Biao Shi, Xin Yao, Fuhua Hou, Sheng Guo, Yucheng Li, Changchun Wei, Yi Ding, Yuelong Li, Ying Zhao, and Xiaodan Zhang. Unraveling the passivation process of pbi2 to enhance the efficiency of planar perovskite solar cells. *The Journal of Physical Chemistry C*, 122(37):21269–21276, 2018.

[32] Zhaoning Song, Changlei Wang, Adam B Phillips, Corey R Grice, Dewei Zhao, Yue Yu, Cong Chen, Chongwen Li, Xinxing Yin, and Randy J Ellingson. Probing the origins of photodegradation in organic–inorganic metal halide perovskites with time-resolved mass spectrometry. *Sustainable Energy & Fuels*, 2(11):2460–2467, 2018.

[33] Waqas Siddique Subhani, Kai Wang, Minyong Du, and Shengzhong Frank Liu. Goldschmidt-rule-deviated perovskite cspbibr2by barium substitution for efficient solar cells. *Nano energy*, 61:165–172, 2019.

[34] Senthilarasu Sundaram, David Benson, and Tapas Kumar Mallick. Chapter 3 - potential environmental impacts from solar energy technologies. In Senthilarasu Sundaram, David Benson, and Tapas Kumar Mallick, editors, *Solar Photovoltaic Technology Production*, pages 23–45. Academic Press, 2016.

[35] Alexander D Taylor, Qing Sun, Katelyn P Goetz, Qingzhi An, Tim Schramm, Yvonne Hofstetter, Maximillian Litterst, Fabian Paulus, and Yana Vaynzof. A general approach to high-efficiency perovskite solar cells by any antisolvent. *Nature communications*, 12(1):1878, 2021.

[36] UNFCCC. The paris agreement. Publication, 2018. Publication date: 29th November 2018. Document type: Publications. Conference: Paris Climate Change Conference - November 2015. Session: COP 21. Topic: Policies and measures.

[37] United States White House. Fact sheet: President biden sets 2030 greenhouse gas pollution reduction target aimed at creating good-paying union jobs and securing u.s. leadership on clean energy technologies, 2021. Accessed on: Insert Date Here.

[38] U.S. Department of Energy (DOE). On the path to 100% clean electricity - final report, May 2023. Accessed: Insert Date Here.

[39] U.S. Energy Information Administration (EIA). Electric power annual 2023. https://www.eia.gov/electricity/annual/, 2023. Accessed on: Insert Date Here.

[40] Liangbin Xiong, Yaxiong Guo, Jian Wen, Hongri Liu, Guang Yang, Pingli Qin, and Guojia Fang. Review on the application of sno2 in perovskite solar cells. *Advanced Functional Materials*, 28(35):1802757, 2018.

[41] Junwen Yin, Gilberto Teobaldi, and Li-Min Liu. The role of thermal fluctuations and vibrational entropy for the delta-to-alpha transition in hybrid organic-inorganic perovskites: the fapbi3 case. *arXiv preprint arXiv:2201.05419*, 2022.

[42] Raneen Zahran and Zafer Hawash. Fullerene-based inverted perovskite solar cell: A key to achieve promising, stable, and efficient photovoltaics. *Advanced Materials Interfaces*, 9(35):2201438, 2022.

[43] Dewei Zhao, Yue Yu, Changlei Wang, Weiqiang Liao, Niraj Shrestha, Corey R Grice, Alexander J Cimaroli, Lei Guan, Randy J Ellingson, and Kai Zhu. Low-bandgap mixed

tin–lead iodide perovskite absorbers with long carrier lifetimes for all-perovskite tandem solar cells. *Nature Energy*, 2(4):1–7, 2017.